

Separate and Detailed Characterization of Signal and Noise Enables NMR Under Adverse Circumstances

A. Guinness,¹ Alec A. Beaton,¹ and John M. Franck¹

¹*Department of Chemistry, Syracuse University, Syracuse, NY 13210, USA**

(Dated: Tuesday 29th October, 2024)

When deploying a spectrometer in an adverse environment, such as during a typical ODNP experiment or other experiments that require low-volume low-field measurements, a clear and modern protocol for characterizing and quantifying the absolute signal and noise levels proves essential. This paper provides such a protocol. It also highlights the clarity and insight that come from (1) characterizing the spectral distribution of the noise, and (2) discussing NMR signal intensities in (conserved) units of square root power. Specifically, the signal intensity is derived from a theory and notation that combine elements of those developed for NMR and ESR spectroscopy, while the spectral noise density “fingerprint spectrum” can identify sources of electromagnetic interference (EMI) and definitively confirm which solutions do and do not mitigate the EMI.

The protocol introduced here should apply to a wide range of instruments, and should prove especially useful in cases subject to design constraints that require integration with multiple other modules that are not dedicated to NMR but that control other forms of spectroscopy or other crucial aspects of the measurement. This protocol demonstrates firstly that quantitative characterization of the noise spectral density allows the identification of successful noise mitigation techniques and secondly that the absolute signal can be accurately estimated from the theory, allowing a systematic approach to instrument design and optimization. For the specific X-band ODNP design demonstrated here (and utilized in other laboratories), the theory then identifies the inefficient distribution of fields in the hairpin loop probe as the main remaining bottleneck for the improvement of low-field, low-volume ODNP SNR.

I. Introduction

New physical techniques and modern technologies are reinvigorating the magnetic resonance community. This is especially true of low-field NMR. For example, ODNP performs detailed analyses of hydration dynamics on the surfaces and interiors of samples with intricate structure at the nanoscale: ranging from proteins to porous materials [1–10]. ODNP extends to applications outside of hydration dynamics as well including resolving ¹H chemical shift differences [11, 12], studying structural transitions [13], assisting in “diagonal” suppressed homonuclear 2D correlation [14], studying the performance of potential polarizing agents [15], and interrogating the time course of nuclear spin polarization buildup [16]. However, it imposes specific requirements on the experimental setup. In particular, while integration with a standard cw ESR spectrometer offers clear advantages, it is reasonably well recognized that standard ESR instrumentation introduces a sea of noise that renders the isolation and optimization of signal increasingly difficult. ODNP thus serves as a good example of what can be termed “NMR under adverse circumstances.” It serves as a case study for a field that includes a diverse set of applications: single-sided NMR for materials studies [17], NMR in the presence of electromagnetic noise [18], NMR in oil bore wells [19, 20], NMR techniques in hydrogeological investigations [18, 21, 22], and portable NMR [23].

While the realm of low-field NMR, generally, and even X-band ODNP specifically, has become quite crowded

with the development of an ever-increasing array of designs to resolve this issue, the authors are aware of few clear and robust protocols to aid in the development of these designs. This situation is exacerbated by the fact that actions that solve noise issues on one system (*e.g.* for ODNP), such as adding hardware to ground transmission lines to the waveguide [1, 6, 24], changing the model of the commercial electromagnet power supply [25], deriving magnetic field from permanent magnets [11, 12, 17, 26], or developing customized hardware [11, 12, 27] do not yield the same success in different laboratory environments. Practically, even the best new hardware designs in the literature might not be compatible with the requirements, capabilities, or environment of a different laboratory.

Similar problems have been seen in other techniques such as atomic force microscopy. One previously presented solution [28] that is treated as a prime method for noise analysis [29], utilizes the power spectral density to isolate environmental noise from the frequency noise induced by molecular motions. This technique facilitated drastic decreases to the sample-related force noise and frequency noise in magnetic resonance force microscopy [30].

Meanwhile, the optimization of signal to noise in the NMR community can often be treated as an art. A variety of strategies are available, including utilization of pre-polarization pulses [22, 31], incorporation of better shielding [26, 30, 32–35], active shielding of low frequency noise [36], improved grounding [33], additional shim coils [12], and improved amplifier noise figures [37–39], while the post-processing stage of data analysis is

* jmfranck@syr.edu

also implemented to improve the SNR [21, 40–44]. The fundamental science governing the SNR is well established, but is frequently presented with design-specific details that distract from the essential clarity that can be synthesized from a couple seminal papers (Hoult [45] and Mims [46]). As a result, the NMR community requires not just new instrumental schematics, but also (as provided here) a simple, flexible, and fundamentals-driven protocol for both systematically diagnosing and mitigating the sources of noise and for identifying the elements of the design that limit the absolute signal intensity.

This paper begins with a theory section (Sec. II) then the results are arranged in the order of the recommended protocol: First, common off-the-shelf equipment, especially when coupled with open-source software, can easily characterize the noise over a broad bandwidth (Sec. IV.1.A). Digitization of the noise power spectral density identifies the relative contribution of various noise sources in the laboratory according to their respective spectral fingerprints (Sec. IV.1.C). Noise mitigation efforts can then be reproducibly tested until the noise approaches the thermal noise limit (Sec. IV.1.F). Characterization of the receiver response then leads to quantitative agreement between the noise measured on the receiver *vs.* with standard off-the-shelf equipment (Sec. IV.2.B). In particular, this allows identification and correction for the idiosyncrasies of the receiver, and avoidance of extra noise introduced by the receiver (Sec. IV.2.C). Finally, the adapted theory can make a very accurate prediction of the signal that will be observed in the customized system, and can also identify the most promising next steps (Sec. IV.3).

II. Theory

This section first presents equations for NMR signal intensity based on relatively few assumptions. In particular, it emphasizes that a great deal of conclusions can be derived exactly if two principles are combined: (1) the concept of reciprocity (from Hoult [45], Sec. II.2) and (2) the relationship between the stored energy and the definition of the Q -factor (from Mims [46], Sec. II.3). These concepts integrate most naturally with the aid of a definition from the ESR literature: the conversion factor (Λ , Sec. II.1). The theory also reviews the concept of Johnson-Nyquist noise (Sec. II.4). Finally, because part of the results emphasize the benefit of characterizing the power spectral density of the noise, the theory section provides equations to generate such plots from data acquired on a standard digital capture oscilloscope (Sec. II.5).

II.1. The Conversion Factor

The term the ESR literature denotes as the “conversion factor” (i.e., “efficiency parameter”) [47–50], Λ , with units $[\text{T}/\sqrt{\text{W}}]$, gives the ratio of the rf magnetic field to the pulse power:

$$\Lambda = \frac{B_{1,avg}}{\sqrt{P_{tx}}} \quad (1)$$

where P_{tx} ([W]) is the average transmitted power required to achieve a rotating frame magnetic field of $B_{1,avg}$ (where $B_{1,avg}$ [T] is averaged over the sample) [48–50]. By applying the simple relationship, $B_{1,avg} = \frac{\theta}{\gamma t_p}$ where θ is the tip angle [rad], γ is the gyromagnetic ratio $[\text{rad} \cdot \text{s}^{-1} \cdot \text{T}^{-1}]$, and t_p [s] is the pulse length required to achieve θ , one sees that the value of Λ can be determined from a standard calibration of the 90° pulse time, namely:

$$\Lambda = \frac{\pi}{2\gamma t_{90}\sqrt{P_{tx}}} \quad (2)$$

where t_{90} [s] gives the time it takes a pulse of average power P_{tx} to tip the spins from the z -axis into the transverse plane ($\theta = \frac{\pi}{2}$).

II.2. Reciprocity in terms of Λ

With the assumption that the spins are uniformly excited, the peak voltage of the signal (ξ_{sig}) generated during an echo with minimal relaxation can be determined from

$$\xi_{sig} = \left(\frac{B_{1,lab}}{I_{coil,p}} \right) \omega M_0 V_s, \quad (3)$$

where ω is the Larmor frequency [rad/s], V_s is the volume of the sample [m^3], and $B_{1,lab}$ is the average magnetic field [T] that is generated perpendicular to the static field when a current of $I_{coil,p}$ [A] flows through the coil; note that the ratio $B_{1,lab}/I_{coil,p}$ appears in Eq. (3) as a consequence of the principle of reciprocity (derived in Sec. S1.8, consistent with literature [45]). Eq. (3) is equivalent to Eq. 4 of Hoult’s seminal paper on reciprocity [45], assuming $K = 1$. M_0 is the nuclear magnetization which, in the absence of hyperpolarization, is given by

$$M_0 = \frac{N\omega\gamma\hbar^2 I(I+1)}{3k_B T}, \quad (4)$$

where N is the number of spins per unit volume, I is the quantum number of the spin (e.g., $I = 1/2$ for ^1H , 1 for ^2H), and T is the temperature [K] of the sample.

Of course, a lossless matching network attached to the coil will alter this voltage ξ_{sig} , but will conserve the square root of the peak signal power

$$\sqrt{P_{sig}} = \frac{\xi_{sig}}{\sqrt{R_{coil}}} = \left(\frac{B_{1,lab}}{I_{coil,p}} \right) \frac{\omega M_0 V_s}{2\sqrt{R_{coil}}}, \quad (5)$$

where R_{coil} is the resistance of the coil. Because power is conserved, the same $\sqrt{P_{sig}}$ will be measured at the terminals of any lossless matching network (Fig. 1a). Note there is an equal voltage drop (of $\xi_{total}/2$) across the lossy elements of the probe and the transceiver [51] in Fig. 1 resulting in the factor of two in the denominator of Eq. (5). Furthermore, a collection of terms in Eq. (5) can be substituted with the conversion factor (Λ) by noting that the

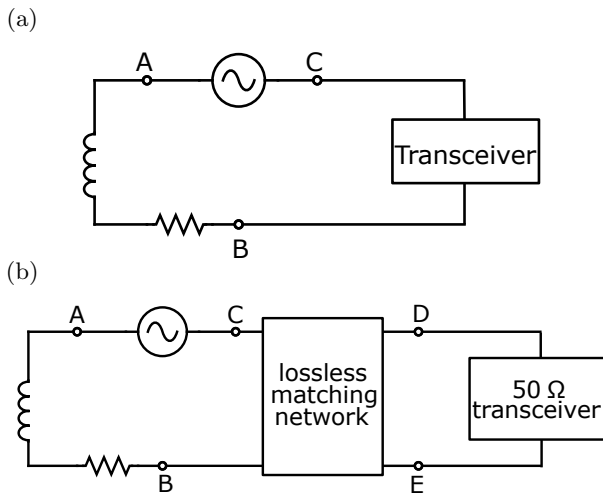


FIG. 1. Example of a coil in a(n): (a) ideal scenario where the coil is matched perfectly to a detector with no matching network required. The voltage loss between points A and B (across the coil components) is equal to the voltage loss between points C and D on the side of the detector. (b) circuit that contains a lossless matching network between the coil and the detector, transforming the impedance of the coil to match the transceiver (50 Ω). In this case, the voltage drop from A to B is equal to the voltage loss from D to E.

only source of resistive impedance in a circuit such as the one illustrated in Fig. 1a, is R_{coil} , and thus

$$\frac{B_{1,lab}}{I_{coil,p}\sqrt{R_{coil}}} = \frac{(2B_{1,avg})}{(2\sqrt{2}I_{coil,rms})\sqrt{R_{coil}}} = \frac{1}{\sqrt{2}}\Lambda, \quad (6)$$

where $B_{1,lab} = 2B_{1,avg}$ accounts for the two counter-rotating components of the magnetic field, while $I_{coil,rms} = I_{coil,p}/\sqrt{2}$ converts from current amplitude to rms current. Eq. (5) then becomes

$$\sqrt{P_{sig}} = \frac{1}{\sqrt{2}}\omega M_0 V_s \Lambda. \quad (7)$$

This expression also holds for any circuit equivalent to Fig. 1b, since the attenuation will decrease Λ equally in the context of the pulse generated and of the signal detected. Eq. (7) quantifies in a more convenient form what is already stated by Hoult [45] and well-known in ESR spectroscopy:

Λ is not merely an expression of how efficiently the probe converts pulse power into magnetic field, but also determines the amplitude of the signal that the probe will generate.

II.3. Factors affecting Λ

Having established the centrality of the conversion factor (Λ) as a figure of merit for probe design, a careful analysis of existing literature (both NMR and ESR) concludes that only three quantities control the value of Λ : the volume of the sample, the Q -factor, and the “field distribution factor” η' (a precisely defined quantity that

takes the place of previous approximations for the filling factor).

On resonance, the probe oscillates between storing the same amount of energy as magnetic and electric field energy. As noted by Mims [46], the energy stored in an impedance-matched resonant rf circuit can thus be *exactly* quantified with the relation:

$$\frac{1}{2\mu} \iiint |\mathbf{B}_1(\mathbf{r})|^2 d\mathbf{r} = \frac{QP_{tx}}{\omega} \quad (8)$$

where the three dimensional \mathbf{r} integral spans all space (excluding fields inside the matched transmission line), ω is the resonance frequency, and P_{tx} is the average power that generates the \mathbf{B}_1 field. The left-hand-side of Eq. (8), is a standard expression for magnetic field energy, while QP_{tx}/ω gives the energy stored inside the resonator, based on the definition of Q (ratio of energy stored to energy dissipated per radian) and the fact that a matched resonator must be dissipating P_{tx}/ω Joules of energy per radian [46]. Eq. (8) defines $\mathbf{B}_1(\mathbf{r})$ distinctly from $B_{1,avg}$ in Eq. (1) and integrates over all magnetic fields generated by all circuit elements within the impedance matched probe. $B_{1,avg}$ represents the average only over the portion of the rf field capable of generating nutation:

$$2B_{1,avg} = \frac{1}{V_s} \iiint_{V_s} \frac{|\mathbf{B}_0(\mathbf{r}) \times \mathbf{B}_1(\mathbf{r})|}{|\mathbf{B}_0(\mathbf{r})|} d\mathbf{r} \quad (9)$$

where the vector \mathbf{B}_0 is the static magnetic field [52].

Mims’ analysis [46] was developed for resonators that even lacked well-defined lumped circuit elements. In various contexts, such an analysis can offer crucial insight; for example, many X-band ODNP setups employ a hairpin loop coil with a very small inductance that one can suspect suffers competition from stray inductances within the rest of the tuning circuitry. A traditional definition of the “filling factor” (η) frequently refers to the extent to which a sample fills a sample coil ([53]), although the very earliest NMR literature acknowledges that this term is actually defined from first principles in terms of the distribution of the magnetic field [54–56]. There are many variations on this definition in an attempt to more accurately estimate probe sensitivity [57–61]. However, by integrating elements from Mims’ analysis [46], one can see that the definition

$$\eta' = \frac{4B_{1,avg}^2 V_s}{\iiint |\mathbf{B}_1(\mathbf{r})|^2 d\mathbf{r}} \quad (10)$$

proves more general and/or accurate than other options. The value of η' is unitless: both the numerator and denominator have units of $[\text{T}^2 \cdot \text{m}^3]$ (with field in the lab frame). In the idealized case where the only rf magnetic field that exists outside the transmission line is a uniform field amplitude of $2B_{1,avg}$ that exists only inside the coil volume, then η' would correspond to the extent to which the sample fills the inside of the coil: *i.e.* under such

idealized (and non-physical) conditions, one would find $\eta' \rightarrow V_{sample}/V_{coil}$. However, as the results will indicate, very constrained designs such as the hairpin loop utilized in many ODNP experiments fall very far from this condition.

With regards to the definition of η' , some historical comparison and contrast may prove fruitful. Note that the definition of η' is very similar to that of the “magnetic filling factor” [57], but to distinguish from many other, subtly different definitions of filling factor, and to choose a more accurate terminology, η' is referred to here as the “field distribution factor.” Note that it corresponds exactly to the quantity V_s/V_c in Mims’ (and therefore much ESR) nomenclature [46]. Assuming that the definition of “effective resonator volume” in ESR literature matches that of Mims, several definitions of “filling factor” in ESR literature [60, 62, 63] in fact match the definition of the field distribution factor almost exactly. Crucially, however, note that the original “ V_c ” of Mims (exactly equal to V_s/η') is an “effective cavity volume” that is defined as the volume integral of $|B_1(\mathbf{r})|^2/(2B_{1,avg})^2$. Unlike in Abragam and others, it is distinct from the coil volume (pg. 74 of [64]). Rather, it gives the effective volume over which the field is distributed, and it is never equal to the volume of a coil, cavity, or any other physical object.

Some simple substitutions offer further insight into the nature and importance of η' . First, substitution of Eq. (8) into Eq. (10), yields

$$\eta' = \frac{2\omega B_{1,avg}^2 V_s}{\mu Q P_{tx}}. \quad (11)$$

Note this expression relies on few assumptions, being simply a ratio between the (Joules of) energy that would be required to generate a rotating-frame $B_{1,avg}$ under idealized circumstances ($2B_{1,avg}^2 V_s/\mu$), and the total energy stored in the probe, $Q P_{tx}/\omega$. Substitution of Eq. (1) simplifies and relates η' to Λ :

$$\eta' = \frac{2\omega V_s \Lambda^2}{\mu Q}. \quad (12)$$

Rearranging Eq. (12) yields an equation that decomposes the conversion factor (Λ) into contributions from the field distribution factor (η'), the Q -factor, and the volume of the sample:

$$\Lambda = \sqrt{\frac{\mu \eta' Q}{2\omega V_s}} \quad (13)$$

This expression explains how to optimize the sensitivity of the probe, and it therefore naturally resembles many equations that one finds in the probe design literature [57, 59]. However, as a result of following the analysis of Mims [46] and the resulting definitions, Eq. (12) is exact and can be generalized to unusual probe designs – in fact, to any impedance-matched rf resonator. Substituting Eq. (13) into Eq. (7) to yield

$$\sqrt{P_{sig}} = \frac{1}{2} M_0 \sqrt{\mu \omega \eta' Q V_s} \quad (14)$$

particularly emphasizes that more efficiently distributing the magnetic field (increasing η'), decreasing the loss of the circuit (increasing Q), or increasing the sample volume (increasing V_s), will all have equivalent effects on the signal amplitude. Furthermore, improvement in any one of these factors will allow for the same SNR with proportionately less signal averaged transients (as $\text{SNR} \propto \sqrt{\# \text{ transients}}$). Because the needs of the application typically dictate the resonance frequency, the number of scans that are possible, and the volume of the sample, the probe designer concerns themselves with optimizing the field distribution η' and the Q -factor.

Finally note that a measurement of the Q -factor, and the t_{90} at a specific power (P_{tx}) provides sufficient information that one can deduce the value of the field distribution factor (η') without relying on any approximations or assumptions. Specifically, substitution of Eq. (2) into Eq. (12) shows that the field distribution factor:

$$\eta' = \left(\frac{\pi^2}{2\mu\gamma^2} \right) \left(\frac{\omega V_s}{Q t_{90}^2 P_{tx}} \right) \quad (15)$$

is a function of physical constants (μ and γ) and quantities that one can measure (ω , t_{90} , Q , P_{tx} and V_s).

II.4. Johnson-Nyquist Noise

Of course, this article concerns itself, in part, with the origins of noise that can obscure low-field NMR signal. The Johnson-Nyquist noise [65] that a receiver chain detects when connected to an impedance-matched probe is given by [59]:

$$\frac{P_{noise}}{\Delta\nu} = k_B T \quad (16)$$

where k_B is Boltzmann’s constant [J/K], T is the temperature [K], and $\Delta\nu$ is the bandwidth [Hz] of the detector. In contrast to 1/f noise from active components or EMI from other instruments in the environment, the Johnson-Nyquist noise is white noise – *i.e.*, does not vary with frequency [29, 37].

Of course, low-noise amplifiers will also add a noise level consistent with their noise temperature, as governed by the Friis equation,

$$F_{total} = F_1 + \frac{F_2 - 1}{G_1} + \frac{F_3 - 1}{G_1 G_2} + \dots + \frac{F_n - 1}{G_1 G_2 \dots G_{n-1}} \quad (17)$$

where F_n is the noise factor of the n^{th} stage of a multistage amplifier, and G_n is the gain of the n th stage of the multistage amplifier [66]. As a large portion of the results focus on identifying and reducing EMI; we refer to the noise that results from Eq. (16) and the LNA noise (Eq. (17)) as the “thermal noise limit.”

II.5. Standard Equations for Signal Processing

Several equations assist in relating real-valued oscilloscope data to quadrature data and/or noise power spectral densities.

The standard analytical signal transformation effectively converts real-valued signal $s(t)$ into analytic signal $s_a(t)$. Specifically,

$$\tilde{s}(\nu) = \sum_{j=0}^{N-1} e^{-i2\pi\nu j\Delta t} s(j\Delta t)\Delta t \quad (18)$$

$$s_a(t) = \sum_{j=0}^{N-1} (2 - \delta_{\nu,0}) e^{+i2\pi j\Delta\nu t} \tilde{s}(j\Delta\nu)\Delta\nu \quad (19)$$

where Δt is the spacing between the time domain points, N is the number of data points (and $t_{acq} = (N-1)\Delta t$ is the acquisition length), $\delta_{\nu,0}$ is zero except at $\nu = 0$ (where it is 1), and the spacing between the frequency domain points is given by $\Delta\nu = 1/N\Delta t = 1/(t_{acq} + \Delta t)$. (Eq. (19) corresponds to multiplication in the frequency domain by a Heaviside function and downsampling.) The analytic signal provides instantaneous amplitude ($|s_a(t)|$), power ($|s_a(t)|^2$), and phase ($\text{angle}(s_a(t))$) information, while

$$\Re[s_a(t)] = s(t) \quad (20)$$

(with $s_a(t)$ sinc interpolated to twice the sampling rate) corresponds to the signal captured on the oscilloscope.

Note specifically that the average power of an arbitrary analytic signal is then

$$P_{avg} = \frac{1}{2Z_c t_{total}} \int_0^{t_{total}} |s_a(t)|^2 dt, \quad (21)$$

where Z_c is the characteristic impedance [Ω], and t_{total} is the duration of the analytic signal. When considering an rf signal with constant amplitude, from Eq. (20), the complex magnitude of the analytic signal $|s_a|$ will be equal to the rf amplitude. Thus Eq. (21) becomes $P_{avg} = \frac{|s_a|^2}{2Z_c}$. Pointing out that $|s_a|/\sqrt{2}$ is equivalent to the rms voltage may allow the reader to see the equivalence between Eq. (21) and more well-known expressions.

Furthermore, the analytic signal derived from the oscilloscope data corresponds to signal digitized on a quadrature digital receiver ($s_{rx}(t)$),

$$s_{rx}(t) = (s_a(t) \exp(-i2\pi\nu_c t)) \otimes f_{DF}(t) \quad (22)$$

where ν_c is the carrier frequency of the NMR signal (the digital equivalent of a local oscillator (LO)), $f_{DF}(t)$ is the time-domain convolution filter that is applied by the digital receiver, and \otimes represents the convolution operation.

Even though noise is, of course, phase incoherent, the power of the noise ($P_{noise}(\nu) \propto |\tilde{s}(\nu)|^2$) still adds linearly, allowing for the signal averaging and/or convolution that are important to clarifying the shape of P_{noise} and deriving meaning from it. Specifically, the complex magnitude of the Fourier transform of time-domain noise acquired by an oscilloscope or digital receiver is divided by the characteristic impedance and the length of the acquisition to convert to a PSD ($P_{noise}(\nu)$) with units [W/Hz].

A convolution (normalized Gaussian of width σ) in the frequency domain also smooths the data:

$$\begin{aligned} P_{noise}(\nu) &= \frac{1}{t_{acq} Z_c \sigma N \sqrt{2\pi}} \sum_{i=1}^N \sum_{j=0}^{N-1} e^{-(\nu-j\Delta\nu)^2/2\sigma^2} \\ &\quad \times \left| \sum_{t=0}^{t_{acq}} e^{-i2\pi\nu' t} n_i(t) \Delta t \right|^2 \Delta\nu \\ &= \frac{1}{t_{acq} Z_c \sigma N \sqrt{2\pi}} \sum_{i=1}^N e^{-\nu^2/2\sigma^2} \\ &\quad \otimes \left| \sum_{t=0}^{t_{acq}} e^{-i2\pi\nu t} n_i(t) \Delta t \right|^2 \end{aligned} \quad (23)$$

where $n_i(t)$ [V] is the time-domain noise voltage, Z_c [Ω] the characteristic impedance of the transmission line (typically 50 Ω), t_{acq} [s] the length of the acquisition, σ [Hz] the convolution width, and N is the number of averaged scans. Here, scripts that store data to disk always convert the (real valued) oscilloscope data to analytic signal *via* Eq. (19).

III. Methods

III.1. Samples

A 4.38 μL sample of 27 mM 4-hydroxy-2,2,6,6-tetramethylpiperidine-1-oxyl (TEMPO, Toronto Research Chemical), prepared in deionized water, was loaded into a capillary tube with an inner diameter of 0.6 mm and outer diameter of 0.8 mm, and flame sealed for use as the standard sample, with a typical relaxation time of about 100 ms.

III.2. Hardware

Roughly following the design shown in [24], the tuning box containing adjustable capacitors for the probe's circuit attaches to the bottom of the ESR cavity (which has a threaded connector) by way of a threaded collar piece that presses against a conductive neck protruding from the tuning box. The threaded collar thus brings the tuning box into electrical contact with the shield surrounding the ESR cavity. A multimeter was used to perform a continuity check between the ground of the ESR cavity and the ground of the probe.

As Fig. 2 shows, the ESR cavity sits between the plates of the electromagnet, attached to a waveguide. The bottom of the probe's tuning box connects *via* BNC connectors and 50 Ω coaxial cable (RG58/U 20 AWG) to the input of an aluminum enclosure containing the receiver chain (yellow box in Fig. 2). The receiver chain comprises a home-built passive duplexer, two standard LNAs (MiniCircuits ZFL-500LN+), a low-pass filter (MiniCircuits SLP-21.4+) and (for select measurements) a high-pass filter (Crystek Corporation CHPFL-0010-BNC). Note, that all coaxial cabling presented in Fig. 2 is 50 Ω with BNC connectors. When employed, common-mode chokes of the snap-on Ferrite style (broadband operation up to 300 MHz, 6.35 mm i.d., 12.2-19 mm o.d.) attach to the coaxial cable connecting the tuning box to the receiver

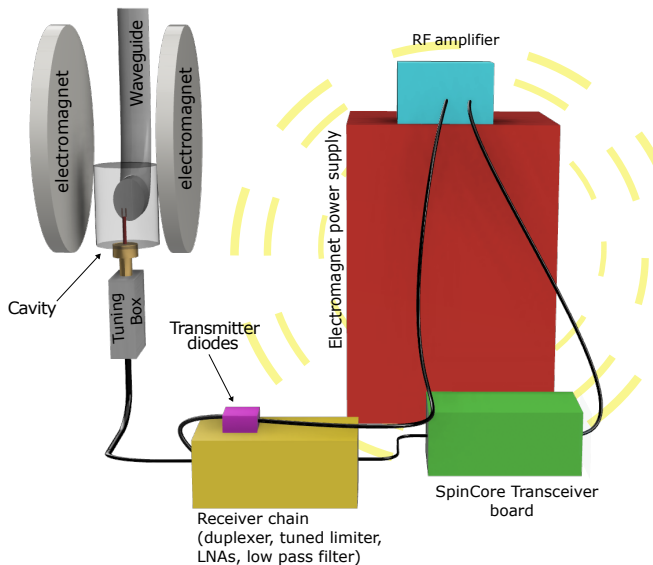


FIG. 2. Instrumental setup: The power supply of the electromagnet (red) sits adjacent to the magnet itself, connected by heavy-gauge DC supply lines (not shown). The RF amplifier (blue box) outputs pulses to the transmitter diodes (pink box), which in turn connect via cable to a tee connector at the input of the receiver chain (yellow). The silver box labeled “tuning box” contains the capacitors for the probe circuit, with the hairpin loop rf coil extending upwards through a hole into the ESR cavity. A cable connects the NMR probe to the tee connector at the front of the receiver chain before the transceiver (combined transmitter/pulse-programmer and receiver) board (green) digitizes it. The electromagnet power supply emits interference noise as indicated by the yellow dashed circles. This drawing omits the microwave amplifier and parts of the ESR instrumentation in favor of emphasizing the elements crucial to the protocol.

chain enclosure. Alternately, a 9 foot coaxial cable connecting the tuning box to the receiver chain enclosure threads through a MnZn PC40 toroidal ferrite core (Hondark HK Limited).

The Bruker E500 hardware [67], in conjunction with the XEPR software and a custom script employing the Bruker Python API, controls the magnetic field. It employs a Hall sensor for magnetic field detection.

During typical NMR experiments, the SpinCore RadioProcessor-G serves as the transceiver board (green box in Fig. 2), offering both pulse programming capabilities and a real-time oversampling capability during detection. All communication with the SpinCore transceiver occurs *via* a Python API extension developed by the authors from the C language API and examples supplied by the vendor [68]. Importantly, note that the protocol here applies to a variety of possible receivers that offer oversampling, and is not restricted to the model of the NMR receiver.

The SpinCore transceiver board outputs the desired pulses that are subsequently amplified by a SpinCore RF amplifier (PA75W-M, 75 W RMS, blue box in Fig. 2).

The amplified pulses are then sent via BNC cabling to an aluminum box containing transmitter diodes (pink box in Fig. 2), which are connected with a BNC tee both to the front of the receiver chain and (*via* a 1 m cable or *via* a 3 m cable threaded through a ferrite toroid) to the NMR probe.

Data that requires independent off-the-shelf test and measurement equipment relies on a minimal set of instrumentation: an oscilloscope (GW-Instek GDS-3254, with bandwidths up to 250 MHz and sampling rates up to 5 GSPS), an Arbitrary Function Generator (GW-Instek AFG-2225), and a handheld Vector Network Analyzer (NanoVNA-H, version 3.5).

It is worth noting that every laboratory setup differs in a way that may affect noise generation and transmission, and that in the authors’ lab, by necessity, all the ESR hardware connects to a different circuit (different voltage supply) than the NMR hardware, and a transformer isolates it from the electrical mains supply. Also, while the flooring surface is insulating, it rests over continuous metal sheeting.

III.3. Details of Oscilloscope-Based Noise Measurement

For the widest applicability, this section covers detailed considerations of performing noise PSD measurements with a standard oscilloscope. All data is acquired using the library available at <https://github.com/jmfrancklab/FLinst> that specifically adopts a strategy of enabling python context blocks for the connection to the oscilloscope, and providing the captured data as an object containing all axis coordinate and unit information (in `pySpecData` format). The strategy should be extensible to a wide range of digital capture oscilloscopes, as well as to spectrum analyzers capable of digital capture (in addition to the direct USB RS232 communication employed here, the libraries also offer context blocks for handling GPIB communications over Prologix connectors). The authors have previously provided [5] a demonstration that the same software and oscilloscope employed here are capable of capturing a phase-cycled spin echo.

For an oscilloscope-based measurement of noise, the receiver chain needs to include a low-pass filter (serving both in reducing high frequency noise and as a point of reference for the noise PSD) after the low-noise amplifiers within the receiver chain. The sampling rate of the oscilloscope must then exceed twice the high-frequency edge of the low-pass filter (*e.g.* in Fig. 3 the sampling rate exceeds 70 MHz). A plot of the noise PSD (Eq. (23)) then clearly displays the edge of the low-pass filter, as shown by the red, green, and gold curves in Fig. 3, which was acquired with a 25 MHz low-pass filter in place.

While standard oscilloscope measurements offer an easy comparison to, and smooth transition to, measurements on the NMR receiver, they do suffer the drawback of a limited dynamic range. Therefore, the vertical scale of the oscilloscope requires optimization (as shown in Fig. 3). A small voltage scale (vertically zoomed in) maximizes the difference between the amplified noise

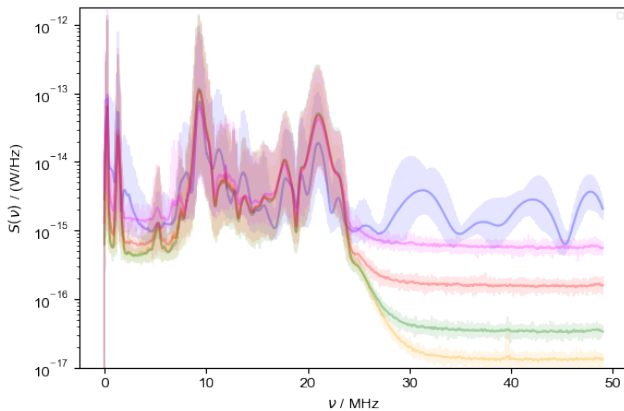


FIG. 3. An oscilloscope set to a sampling rate of 100 MSPS and a voltage scale of 5 (blue), 10 (gold), 20 (green), 50 (red) and 100 mV (magenta), digitized 100 traces of noise acquired from the output end of the receiver chain when hooked up to the tuning box (Fig. 2). In each case, a 100 kHz Gaussian convolution (Eq. (23)) yields a smoothed version of the line direct average, shown as the more transparent line of the same color.

coming from the receiver chain and the intrinsic noise of the oscilloscope that is seen for frequencies above the threshold of the low-pass filter (≥ 30 MHz in Fig. 3). However, a voltage scale that is too small results in a time-domain waveform that is (vertically) clipped, leading to a clear distortion of the PSD (shown in blue). Fig. 3 clarifies this process of dynamic range optimization with data that was acquired in a relatively high-noise configuration. Specifically, a 10 mV voltage scale (gold) maximizes the difference between the intrinsic noise of the oscilloscope and the noise of the receiver chain while still avoiding the clipping-induced distortion seen at 5 mV (blue). Sec. S1.2 includes further details about this dynamic range optimization.

Fig. 3 additionally demonstrates that even after averaging the PSD from 100 captures (acquired in under three minutes) to yield the faint, more transparent lines, these lines still appear broad/thick due to rapid frequency-dependent oscillations in the noise. The Gaussian convolution chosen for broadband measurements (here 100 kHz) smooths out these features to identify general trends in the data while also requiring minimal or no signal averaging in order to produce a smooth and reproducible PSD.

III.4. Generation of Test Signal

A variety of sources can generate a test signal at a fixed voltage and frequency (the results here employ the previously mentioned programmable AFG) which serves as a convenient control case. However, testing with the duplexer in place requires signal at the level of NMR signal – at the μV to nV level, which is much smaller than the minimal output of the average source. Therefore, it becomes necessary to connect precisely cali-

brated attenuators to the output of the frequency source. This is achieved by designating “attenuator assemblies”: the combination of an attenuator with attached cabling and/or adapters that begins with a BNC jack (F) and ends with a BNC plug (M). With the frequency source set to a high voltage, an oscilloscope measures the output of each such assembly to allow calculation of the ratio between the unattenuated voltage and the voltage with the attenuator assembly in place. (A more typical attenuation [dB] value can be used if one takes care to remember the unusual rules for significant figures of logarithmic quantities.) The measurement is repeated several times, to check for variations due to cable positioning.

To generate the test signal, the frequency source is then set to a mV-level voltage (and measured on the oscilloscope), and several attenuator assemblies, which (by design) do not involve insertion losses from any intervening cabling, are then connected as needed. In order to speed this calibration, a simple script captures the oscilloscope data and automatically converts to analytic signal, filters, and measures the rf voltage amplitude (Sec. S1.11).

IV. Results and Discussion

The central result presented here is a protocol that enables detailed characterization and optimization of the absolute signal and noise levels of a custom NMR system. The sections below, in order, outline an example of such a protocol. Over the course of this protocol, the validity and utility of the reorganized theory (Sec. II) are also explored, as well as various specific observations pertaining to the low-field ODNP system investigated here.

IV.1. Noise PSDs from Test and Measurement Equipment

A single unprocessed capture of the noise on the NMR receiver or an oscilloscope tends to yield a relatively uninformative picture, allowing calculation of the standard deviation of the noise voltage and little else [36, 37]. Spectrum analyzers can quantify noise with a high dynamic range, and prove particularly useful for LNA noise factor quantification, while VNAs can identify cross-talk between components (S_{12}) [34, 69–71]. However, both for limiting the necessary instrumentation, and for easier comparison to the NMR receiver, the first steps of this protocol rely primarily on a standard digital oscilloscope to capture the noise that is output by the receiver chain. Eq. (23) then converts the captured time-domain traces to smooth PSDs.

IV.1.A. Intrinsic Noise of the Receiver Chain

The first step of the protocol involves checking that the metal box enclosing the receiver chain provides adequate shielding. The green line in Fig. 4 shows the gain of the receiver chain (measured in Sec. S1.6, Fig. S5) multiplied by the theoretical Johnson-Nyquist noise (Eq. (16)). With a 50Ω terminator attached to its input, the (shielded) receiver chain emits the noise density shown in blue. The noise cutoff at 25 MHz arises from the presence of the low pass filter at the end of the receiver

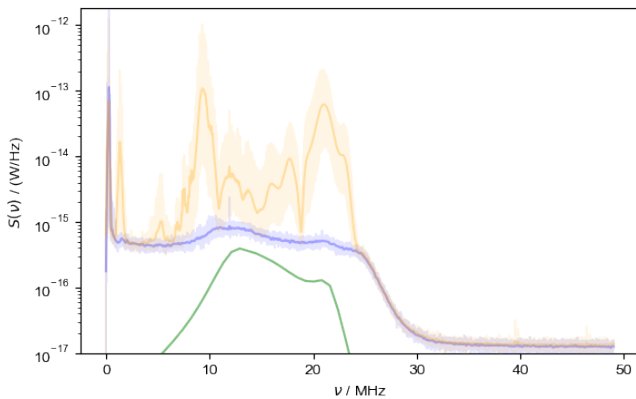


FIG. 4. The noise PSD of the terminated receiver chain (blue) rises slightly above the thermal noise limit (green) over the sensitive range of the duplexer (14-15 MHz). The shape of the thermal noise limit is controlled by the gain of the receiver chain (Fig. S5), which is non-uniform here. When the NMR probe is attached to the input of the receiver chain (gold), very strong EMI is introduced.

chain, while the steep rise at frequencies below 1 MHz comes from $1/f$ noise of the LNAs. At intervening frequencies, the noise density appears approximately flat. The fact that the measured noise *vs.* the thermal noise limit are separated by a factor of ~ 2 , and only for a limited range around the intended resonance frequency of 14-15 MHz, is expected here; the duplexer contains various frequency-sensitive components that filter signal outside the 14-15 MHz range to varying extents, while the LNAs are broadband and will continue to transmit a noise level appropriate for their noise figure (specified as 2.9 dB).

IV.1.B. Noise with Attached Probe

Fig. 4 also highlights a major unexpected issue: attaching the NMR probe to the receiver chain introduces electromagnetic interference (EMI) that exceeds the thermal noise limit by two orders of magnitude. Such high levels of EMI prevent the isolation of small amounts of signal – especially when considering, *e.g.*, the un-enhanced reference scan for an ODNP experiment that comes from a 4.38 μL sample with only thermal (Boltzmann) levels of spin polarization. However, as will be demonstrated in the next step (Sec. IV.1.C), the distinctive shape and frequency specificity of this measurement allows the spectroscopist to systematically identify and mitigate the source of the EMI, identifying it similarly to how one might identify a chemical compound from the fingerprint region of a spectrum.

Note that frequency-domain convolution (Eq. (23)) of the noise PSD proves crucial to developing clear results. As mentioned in Sec. III.3, the apparent thickness of the lines from the un-convolved data (the transparent lines in Fig. 4) arises from high-resolution oscillations. These oscillations make it difficult to extract identifying details like the $1/f$ noise or distinctive frequency varia-

tions arising from particular sources of EMI. The origins of these oscillations will be interpreted later; at this stage in the protocol, however, an empirical observation of the line “thickness” drives the choice of convolution width in Eq. (23) (in Fig. 4, $\sigma = 100$ kHz). Notably, over longer periods of time or when equipment is moved slightly, it is not uncommon for the distribution of the noise density to decrease slightly at some frequencies while increasing slightly at others (not shown). This underscores another important element of the noise measurement protocol introduced here: It is important to start by recording the noise PSD over a broad frequency range. Measures that truly mitigate noise will tend to do so over a broad frequency range. In contrast, exclusively observing noise densities zoomed in to more specific frequency ranges could make it appear that the noise was increasing or decreasing when various changes are made when, on average, it is not.

IV.1.C. Example: Investigating Source of Noise

Many magnetic resonance systems that integrate complex components will have to contend with the resulting added noise contributions such as those seen in Fig. 4. For example, ODNP spectroscopists are relatively familiar with the fact that a commercial electromagnet power supply (here the Bruker E500 system) can emit large amounts of EMI. The protocol here enables a laboratory with almost any level of experience and equipment, access to measure and to confirm the nature of this noise. Fig. 5 expressly shows that the electromagnet power supply introduces EMI that travels through free space and that this EMI exceeds the thermal noise limit by two orders of magnitude. Specifically, the act of turning on the electromagnet power supply (gold \rightarrow green of Fig. 5) introduces the overwhelming majority of the noise that was seen in Fig. 4. Removing the probe from the cavity and placing it on a nearby table breaks any potential direct current path between the probe and the ESR power supply. One would expect that this action would remove any noise brought on by spurious electrical connections, ground loops, *etc.* However, as expected only for EMI traveling through the air, moving the probe out of the cavity yields only a slight decrease of the noise and a redistribution in frequency space.

The following three subsections demonstrate how a reasonably processed broadband noise PSD enables one to systematically choose between a selection of rather simple noise mitigation options, to identify a solution that works well for a particular lab’s experimental needs.

IV.1.D. Test 1: Analysis of Shielding

An implied advantage of the design adapted from Kaminker [24] is that the grounded elements of the probe and cavity would together form a Faraday cage that would shield the probe from EMI. The fact that removing the probe from the cavity and exposing it to the environment (green \rightarrow red in Fig. 5) results in reduced noise is thus surprising.

Therefore, a series of measurements tested the integrity

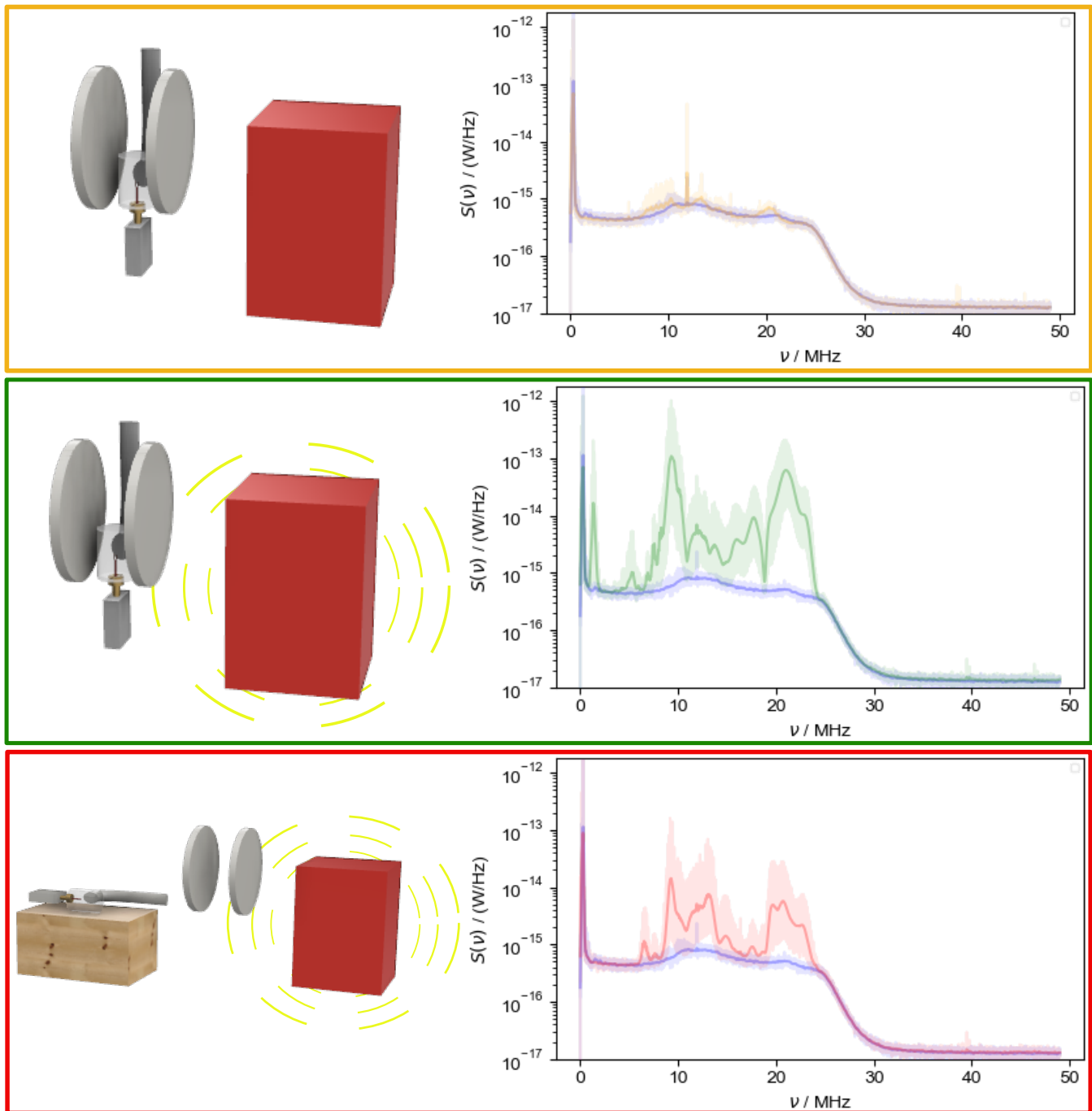


FIG. 5. The noise PSD of the terminated receiver chain (blue line) provides a baseline reference for all plots. All other lines show the noise output by the receiver chain when connected to the NMR probe (grounded to the ESR cavity for gold and green). When the power supply is off (gold), the noise density closely approaches the noise levels of the terminated receiver chain (blue). Turning on the electromagnet power supply introduces dramatic levels of noise (green). Disconnecting the probe from the cavity, and placing it on a table 5 ft from the power supply causes only subtle changes to the noise (red), as discussed in the text.

of the shielding scheme. Three noise PSDs were acquired (Fig. 6): one with the NMR probe secured and properly grounded to the cavity, a second where the probe-cavity-waveguide assembly is detached from the ESR microwave bridge and simply held between the magnets, and a third

where the probe is completely disconnected from the cavity and held between the magnet plates. These PSDs show a lack of a dramatic change in the overall noise density, thus indicating that the cavity likely provides insufficient shielding for the NMR probe.

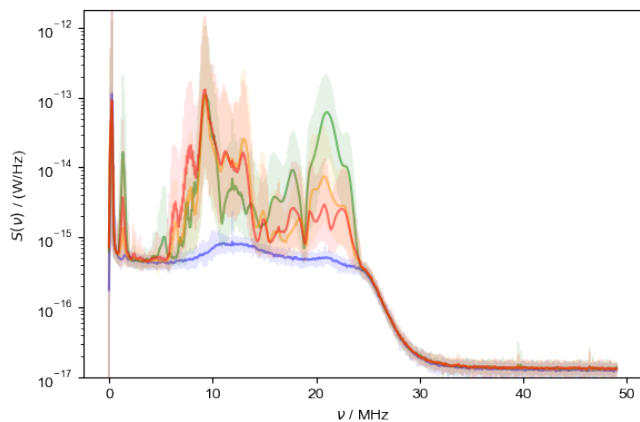


FIG. 6. In the standard configuration (green – same as the configuration for green in Fig. 5), large and distinctive clusters of peaks appear. By detaching the waveguide/bridge connection (gold) the noise at frequencies higher than 13 MHz drop an order of magnitude, but the noise density at some lower frequencies slightly increases. Entirely detaching the NMR probe from the cavity (red) and holding it between the magnets does not yield dramatic changes in the noise density. (Terminated receiver chain noise shown in blue for reference.)

Thus, Fig. 6 identified that improved shielding might prove an effective strategy for noise mitigation. However, optimization of connections between NMR probe and cavity – including improving the metal-to-metal contact between various parts and adding conducting foil over joints – yielded negligible improvement (not shown). Additionally, insertion of a copper plate into the waveguide connection in an attempt to improve the grounding between the NMR probe and the cavity/waveguide assembly (a strategy that was shown to work well in the Han lab [6]), demonstrated no improvement (not shown). While a secondary shielding enclosure may still prove successful for mitigating the EMI noise, this was beyond the scope of basic improvements, and, as shown in subsequent subsections, proved unnecessary.

IV.1.E. Test 2: Balanced Probe Design

A balanced probe design (green circuit in Fig. 7) aims to concentrate the current within the circuit near the coil and to mitigate the antenna effect by approximately equalizing the impedance to ground on either end of the coil [72, 73]. Here, the probe containing a standard tank circuit (gold circuit in Fig. 7) is referred to as the “single-sided tank probe” for contrast. Both coils have an internal volume of 8.6 μL , utilize a double hairpin loop, and integrate specifically into a Bruker Super High Sensitivity Probehead X-Band resonator (ER 4122 SHQE). In addition to the circuitry, the two probes differ in shielding: a thicker 6.5 mm aluminum box encases the single-sided tank circuit while a 1.5 mm thick aluminum box encases the balanced circuit. When the single-sided tank probe is connected in place of the balanced probe (Fig. 7), the receiver picks up slightly less interference noise. Therefore

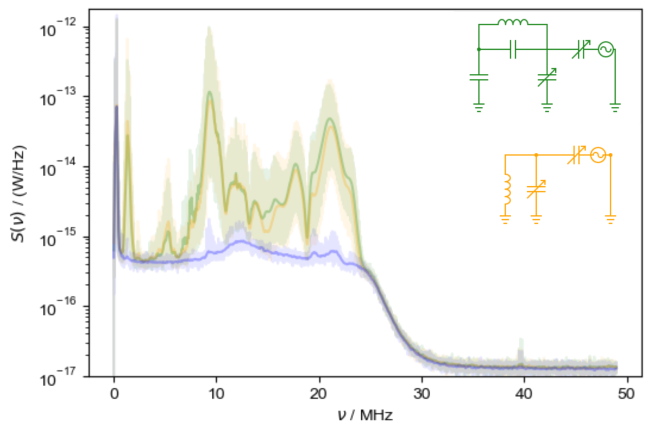


FIG. 7. Different probe circuitry does not aid in preventing EMI pickup. When the DC supply of the Bruker E500 is powered on, the resulting interference noise transmits slightly more efficiently into the balanced NMR probe (green) *vs* the single-sided tank probe (gold). (Terminated receiver chain noise shown in blue for reference.)

all following measurements utilize the single-sided probe.

Fig. 7 emphasizes that the EMI transmitted by the power supply here does not interact solely with the coil; rather, it interacts with the probe and ESR cavity assembly as a whole. The slight differences between the noise PSD of the two probes (Fig. 7) may arise either from the thicker shielding of the single-sided tank probe, or from incidental changes to the rf cross-section of the probe.

IV.1.F. Test 3: Ferrite Chokes Mitigate Electromagnetic Interference

Toroidal ferrite chokes or snap on chokes are a common solution for mitigating high-frequency EMI by selectively increasing the impedance of common mode transmission (associated with noise) while leaving the impedance of the desired transverse (TEM) mode unaltered. Fig. 8 shows how successive addition of snap-on chokes to the coaxial cable connecting the probe to the receiver chain progressively mitigates the EMI in the example system here. However, a toroidal ferrite core can accommodate multiple loops of cable and thus offer a very large common-mode impedance. Simply threading the coaxial cabling around a single toroid produces the same benefit as XX snap on chokes, but with less weight pulling on the cables.

As the noise of the system is decreased, the voltscale should be adjusted to further maximize the difference between the noise of the receiver chain and the intrinsic noise of the oscilloscope (Sec. III.3). Consequently, the noise PSD in Fig. 8 acquired with no form of mitigation (gold) and with a voltage scale of 10 mV, has a seemingly higher level of noise at frequencies greater than the low pass filter threshold compared to the PSDs acquired with chokes applied (which were acquired with voltage scales of 5 or 2 mV). Additionally, while subtle, the noise power of the probe with the chokes present dips below the noise

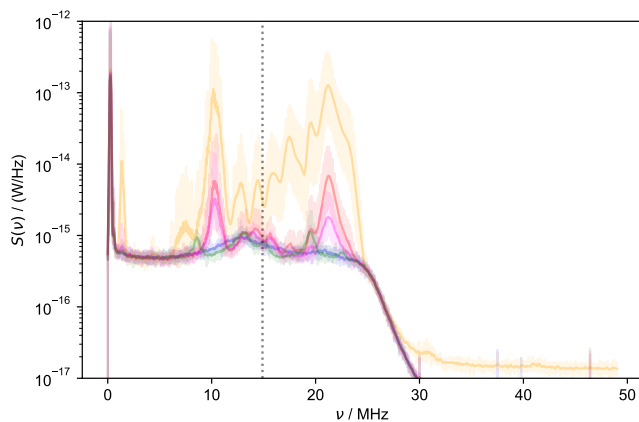


FIG. 8. Common-mode chokes mitigate the EMI, as illustrated by the noise PSD from the standard configuration with 0 (gold – equivalent to the setup shown in green of Fig. 5), 12 (red) and 26 (magenta) ferrite snap-on chokes added to the coaxial cable connecting the probe to the receiver chain. Replacing the chokes with a simple ferrite toroid (green) results in further mitigation of noise. (Baseline noise of terminated receiver chain shown in blue.)

PSD of the terminated receiver chain at frequencies surrounding 14.9 MHz (the frequency which the probe was tuned to with the VNA). This is explained by noting that the reactive capacitance only matches the reactive inductance at the resonant frequency (14.9 MHz). However, at other frequencies, the reactive capacitance does not match the reactive inductance, causing the noise PSD of the probe to dip below the PSD of the terminated receiver chain.

IV.2. Noise PSDs Acquired by NMR Transceiver

There is little quantitative value to the broadband noise PSD measurements unless they correspond to the noise actually digitized on the NMR receiver (transceiver). Therefore, the protocol advocated here next quantifies the noise density on the receiver and compares it to the broadband PSD measurements.

IV.2.A. Receiver calibration

Receivers frequently collect and present acquired data with arbitrary units intrinsic to the board (denoted here as “dg” for “digitizer units”) that must be converted to standard voltage units (V). Initial calibration of the receiver was performed by injecting an rf test signal (Sec. III.4) close to the transceiver carrier frequency with an amplitude of ≈ 15 mV (exact value verified by oscilloscope using Sec. S1.11) directly into the input of the SpinCore transceiver board. A nonlinear fit of the resulting waveform to a complex exponential (*cf.* Eq. (22)), yields the amplitude in [dg]; this is compared to the amplitude in [V] of the same signal measured on an oscilloscope (Fig. S2). For the widest spectral width (75 MHz, the base digitizer frequency), a calibration factor of 6.054 dg/ μ V was measured.

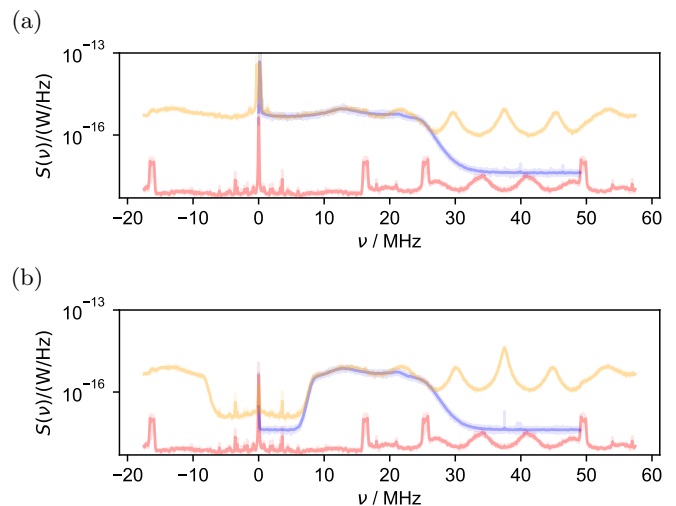


FIG. 9. (a): The PSD of the terminated receiving chain is acquired on the oscilloscope (blue) as well as on the transceiver board with a carrier frequency of 20 MHz and a spectral width of 75 MHz (gold). The noise PSD of the terminated SpinCore (red) shows the intrinsic noise of the transceiver board itself. (b): A high pass filter is inserted into the receiver chain after the low pass filter and the PSD is acquired again both on the oscilloscope and the transceiver board (plotted with the same color scheme as (a)).

IV.2.B. Comparison of Oscilloscope vs Transceiver Noise Measurements

The next step of the protocol here compares the noise PSD from the terminated receiver chain acquired on the NMR receiver to the PSD acquired on the oscilloscope (Fig. 9). Specifically, the SpinCore API Python extension [68] captures a time-domain trace using the same functions that are employed for NMR signal acquisition, with a very wide spectral width (75 MHz, the base digitization frequency). Division by the calibration factor [dg/V] appropriately converts the units to volts. Subsequently, just as for oscilloscope captures, Eq. (23) converts the time-domain data to a PSD.

When digitizing the noise from the terminated receiver chain, the receiver observes approximately the same noise density as the oscilloscope measurements over frequencies less than ≈ 18 MHz. However, at frequencies higher than 20 MHz, the noise PSD of the terminated receiver chain, as acquired on the transceiver board, differs drastically from the PSD acquired on the oscilloscope. Specifically, peaks with a noise density similar to or greater than the noise coming from the receiver chain appear at frequencies ≥ 26 MHz (*i.e.*, above the low pass filter threshold), even though the oscilloscope measurement shows that the receiver chain does not transmit noise in that frequency range. Notably, these contributions are only developed by the transceiver in response to a significant power density of noise. As mentioned in the SI (Fig. S3), these high-frequency noise peaks are found to scale approximately linearly with the input. In the absence of

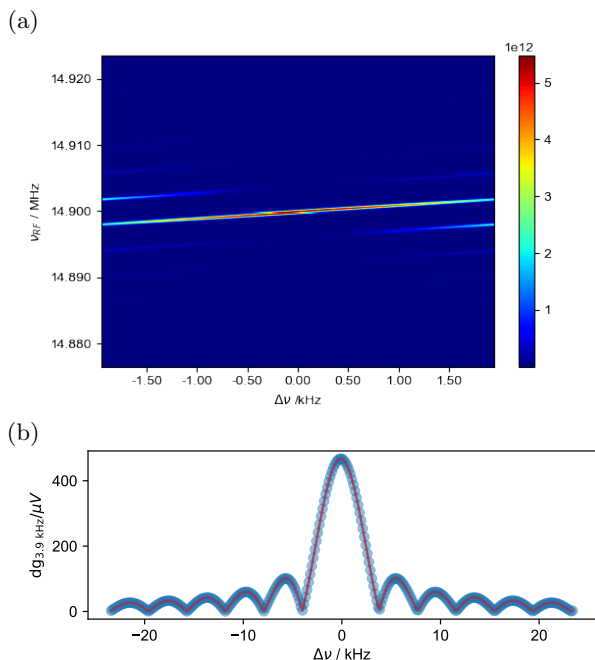


FIG. 10. An AFG outputs varying frequencies of test signal (14.8766 MHz \rightarrow 14.9234 MHz), which the SpinCore receiver board subsequently digitizes with a 14.9 MHz carrier frequency. (a) A 2D plot shows how the intensity of the PSD (a function of the offset, $\Delta\nu$, from the receiver carrier frequency) varies with the frequency of the test signal (ν_{RF}). (b) The maximum of the PSD for each output frequency, acquired on the receiver, is divided by the corresponding maximum of the PSD acquired on the oscilloscope (which is approximately flat – Fig. S5a) and is plotted as a function of the offset from 14.9 MHz. The red line shows the absolute value of a best-fit sinc function.

amplified input (*i.e.* with only a terminator attached to the receiver input), the noise density recorded by the receiver drops several orders of magnitude and changes in frequency (Fig. 9, red). Therefore, the high-frequency noise contributions observed on the receiver board might arise from accidental mixing of the input with internal clock signals, *etc.* Interestingly, as shown in Fig. 9b, addition of a high pass filter does mitigate low-frequency noise, but actually exacerbates the contribution of the internally-generated high-frequency receiver noise peaks. Fortunately, for the X-band ODNP measurements targeted here, only 12-16 MHz carrier frequencies are required; therefore, if the high-frequency peaks can be digitally filtered, they are not of concern.

IV.2.C. Testing Oversampling Performance

Smaller spectral widths yield higher resolution, as longer time-domain traces can be captured and stored using the same on-board memory. With proper oversampling they also exclude noise significantly outside the receiver bandwidth. In the exact context employed here, the default oversampling scheme (specifically $f_{DF}(t)$ in Eq. (22)) was actually unknown. With all receivers,

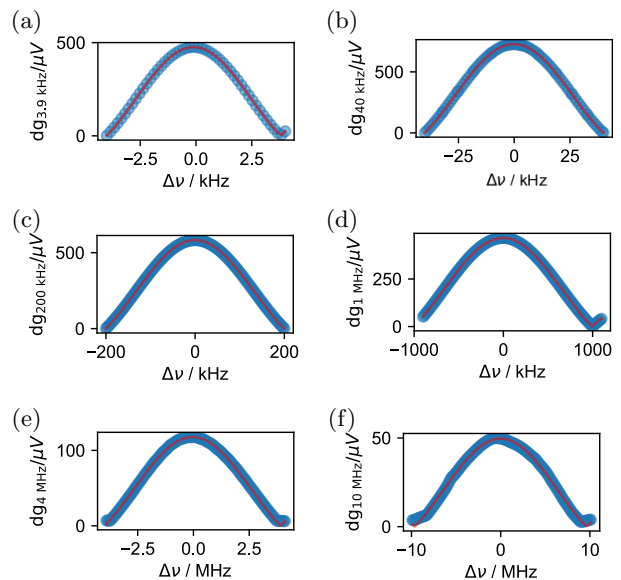


FIG. 11. An AFG outputs test signal at a range of frequencies ($\Delta\nu_{RF} = 2 \times SW$), which the SpinCore receiver board subsequently digitizes with a 14.9 MHz carrier frequency. The maximum of the resulting PSD for each output frequency is plotted as a function of the offset and divided by the actual value of the test signal (which is approximately flat – Fig. S5a) and is plotted as a function of the offset from 14.9 MHz. The transeiver response is plotted for (a) 3.9 kHz, (b) 40 kHz, (c) 200 kHz, (d) 1 MHz, (e) 4 MHz, and (f) 10 MHz.

measuring and validating the oversampling performance proves an essential step to accurately quantifying and optimizing the exact signal and noise power.

To measure the receiver response, a single script (Sec. S1.11.B) varies the frequency of a continuous sine wave test signal (Sec. III.4) with ≈ 5 mV amplitude and captures the response on the receiver. The 2D signal captured on the NMR receiver (Fig. 10a) demonstrates how the receiver does record an alias of signals that exceed the spectral width, and, as expected, the digital filter does decrease the amplitude of these aliases to ultimately negligible levels. The receiver response function quantifying this behavior (Fig. 10b) is determined from the square root of the ratio between the peak of the PSD recorded on the receiver *vs.* the peak of the PSD for the input signal (measured on an oscilloscope). The resulting 1D response plot, shows a good fit to the absolute value of a sinc function, implying that the default oversampling scheme for this NMR receiver is to box-car average the time-domain datapoints. Here, the response specifically fits to a sinc function with a width of twice the spectral width; this characterization holds for all spectral widths (Fig. 11), with only slight deviations for the widest spectral widths. The overall amplitude of the response (here the amplitude of the sinc function) can be determined with greater precision through multiple measurements (Sec. S1.3), resulting in the values given in Table I.

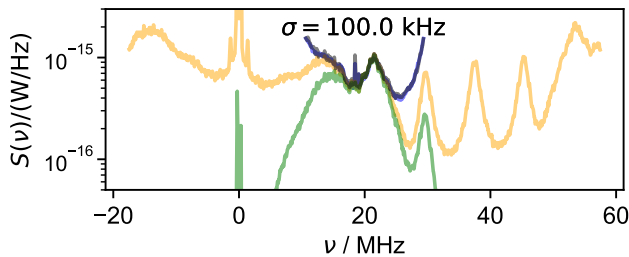


FIG. 12. Eq. (23) converts the digitized captures of the noise for the terminated receiver chain acquired on the receiver with the base sampling rate of 75 MHz, to a PSD (gold). Multiplication of the gold line by a sinc function appropriate for a dataset with a spectral width of 20 MHz yields a filtered noise PSD (green). Subsequent downsampling produces the predicted noise PSD for a spectrum taken with a spectral width of 20 MHz (transparent grey/black). This prediction matches the PSD measured at 20 MHz (blue); note that the transparent black prediction line overlaps the measured line almost exactly, making it appear a dark blue.

IV.2.D. Noise PSDs at Different SW

Full characterization of the response of the NMR receiver (as in Fig. 11) exactly explains the relationship between the noise PSD observed at different spectral widths. Specifically, Figs. 12 and 13 demonstrate that the following procedure can predict the noise density at a smaller SW from the noise density acquired with a larger SW:

1. Convert the time domain trace for the broader SW to a PSD via Eq. (23).
2. Divide by the square of the receiver response [dg/V] specific to the larger SW, yielding the true noise PSD of the broader SW – *e.g.* the gold line in Fig. 13. (In Fig. 12, the response of the gold line is assumed to be approximately flat, since the SW corresponds to the base sampling rate.)
3. Multiply by the square of the response for the smaller, desired spectral width – yielding, *e.g.*, the green lines in Figs. 12 and 13.
4. Move to the time domain (inverse Fourier Transform) and interpolate the data with a cubic spline function (because the faster sampling rate is not always an integer multiple of the slower sampling rate).
5. Sample the interpolation function at the slower sampling rate corresponding to the narrower SW, and move back into the frequency domain – yielding, *e.g.*, the dark grey lines in Figs. 12 and 13 that compare well with the noise density measured at the narrower SW.

This procedure can explain unusual features in the noise density. For example, the small noise spike both observed and predicted near 19 MHz in Fig. 12 arises from aliasing of the $1/f$ noise, as evidenced by the fact that the filtered (green) spike near 0 MHz still has sufficient amplitude

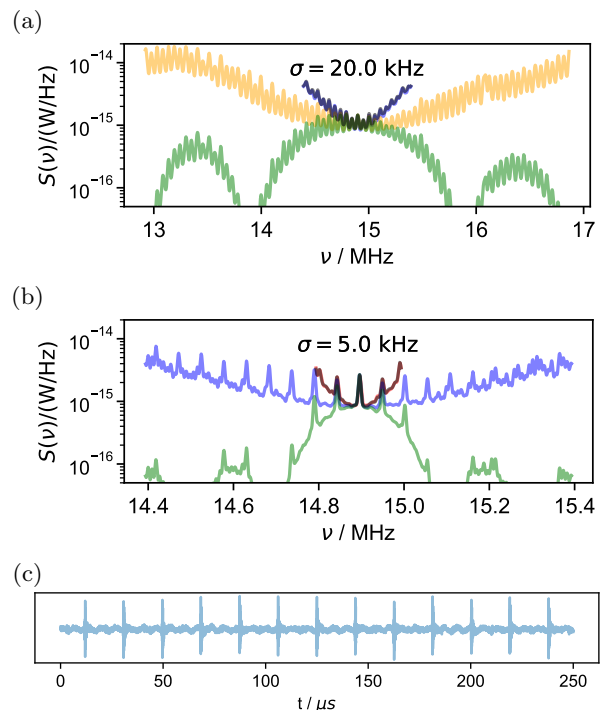


FIG. 13. (a) The measured noise PSD for the probe inserted between the magnets without chokes, acquired with SW = 4 MHz is divided by the square of the 4 MHz response function (see Fig. 11) to yield the gold line. The product of the gold line with the square of the 1 MHz response function yields the green line. Subsequent down-sampling in the time domain (see text) then results in a prediction (transparent grey/black line) that matches well with the measured 1 MHz PSD (blue). Note that the transparent black prediction line overlaps the measured line almost exactly, making it appear a dark blue. (b): The same 1 MHz PSD data shown in (a) (indicating the PSD has already been divided by the square of the 1 MHz response function) convolved by a 5 kHz filter width (blue) is multiplied by the response function for a SW = 200 kHz (green). Downsampling of the green line results in a PSD (transparent grey/black) that accurately predicts the actual 200 kHz PSD (red). (c): Raw capture from the oscilloscope (acquired without noise mitigation) with spikes that repeat every $\sim 20 \mu\text{s} = 1/50 \text{ MHz}$.

to contribute to the PSD after it is filtered and aliased during downsampling.

This process of predicting and observing PSDs of subsequently narrower SWs reveals the impact and importance of the choice of digital filters employed by the receiver board. From the measurements of Figs. 12 and 13, one can observe first that the noise density of the smaller SW always matches the wider SW measurement at the carrier and, second, that the PSDs exhibit a strong upward curvature off-resonance. The first observation – consistency of the PSD at the carrier frequency – depends on the digital filter. Here, the designers of the receiver board have chosen a sinc of width $2 \times \text{SW}$ as the digital filter; it has the property of falling to zero (having

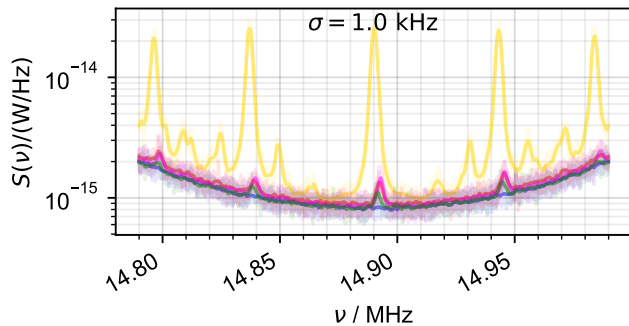


FIG. 14. The noise PSD was acquired at a spectral width of 200 kHz and convolved using a convolution width of 1.0 kHz. The blue line illustrates the Johnson noise of the terminated receiver chain. Similar to fig. 8, gold shows the PSD for the probe inserted into the cavity with the magnet on, and it is clear that magnitudes of noise are introduced. When 12 chokes are added (red) the noise is halved. The addition of 27 chokes (magenta) results in a very minimal decrease in noise compared to the 12 chokes. Replacing the chokes with a toroid (green) results in the largest reduction of noise.

a node) at all offsets equal to an integer multiple of SW (*i.e.*, $n \times SW$). Thus, at zero offset from the carrier frequency, the contributions from all aliases of the filtered signal (*i.e.*, all aliases of the green line in Figs. 12 and 13) fall to zero. For another filter to have no aliased noise at zero offset from the carrier frequency, it must also equal zero for all offsets $n \times SW$. The second observation – the growing increase of the noise PSDs for the more narrow SW upon moving off-resonance – occurs because the sinc filter (and therefore the aliased noise contributions) rises smoothly away from the nodes. With the important caveat that, for many receiver boards, the sinc filter is likely to be the only filter available at a SW close to the base sampling rate (because boxcar averaging in the time domain can be implemented with very few samples), it is worth noting that the upward curvature of the narrow SW PSD would be mitigated by employing an optimized FIR filter (not shown here) that would cause the response to both fall abruptly to zero and remain near zero at the edge of the SW. Note also that, importantly to ODNP and other quantitative methodologies, precise quantification of signals whose offset is a significant fraction of the SW also requires correction by the receiver response function, regardless of whether a boxcar (sinc) or more optimal FIR filter is employed.

IV.2.E. Mitigation of Noise (Observed by the Receiver)

Because oversampling allows the digitization of more noise energy over a smaller bandwidth, it allows Eq. (23) to employ a smaller convolution filter while still measuring a smooth noise PSD, as illustrated in Figs. 13 and 14. Fig. 13 shows the PSD acquired with a 1 MHz SW (blue) using two different convolution widths: 20 kHz, which is more appropriate for the 4 MHz PSD (Fig. 13a), and 5 kHz, which is more appropriate for the higher resolu-

tion 1 MHz (Fig. 13b). Notably, the decrease in convolution width reveals the presence of periodic spikes with a spacing of 50 kHz. As previously alluded to, these periodic spikes contribute to the apparent (vertical) breadth of the un-convolved (transparent) lines in Figs. 3–9. As expected, for cases with high EMI, this feature can also be seen as periodic spikes in the noise signal captured by the oscilloscope – *e.g.*, Fig. 13c. However, the larger convolution widths employed at larger SW (*e.g.*, for the larger SW shown in Figs. 3–9) spread these spikes into each other, contributing to a higher PSD when they are present, even though the individual spikes are not resolved. These spikes, when resolved at smaller SW, rise above a baseline that is not too far above the amplified Johnson noise (9×10^{-16} W/Hz).

As noted previously, the frequency distribution of the EMI does change over the course of a day, and the frequencies of the noise peaks in, *e.g.* Fig. 14 do change in frequency even over the course of minutes or hours, though their intensity tends to remain approximately constant. Therefore, PSD measurements that encompass several such peaks, as in Fig. 14, offer more reproducible comparisons than PSDs acquired at smaller SWs approaching those used for signal acquisition (as in Fig. S4).

In keeping with the improvement shown in Fig. 8, the addition of 12 chokes (gold \rightarrow red in both Figs. 8 and 14) does reduce the large noise spikes from more than an order of magnitude above the baseline, down to a factor of about 2 or 3 above the baseline. The addition of chokes even reduces the baseline level of the PSD (between the intense peaks). Fig. 14 furthermore clarifies that in the range of interest for the current example (14–15 MHz), an increase from 12 to 27 snap-on chokes does not significantly decrease the noise; whereas the broadband measurement in Fig. 8 clarifies that this does decrease the intense noise spikes at other frequencies.

Similar to Fig. 8, the toroid choke removes the same (or even slightly more) amount of EMI noise *vs.* the 27 snap-on chokes in Fig. 14. Acquisition of signal points to another benefit of the toroid: the snap-on chokes occasionally decrease the T_2^* (not shown), while the toroid (located outside the main static magnetic field) does not. A final note is that cable placement and length prove to be an essential component in mitigating EMI noise. For example, further PSD measurements not shown here guided the shortening of the cables between the output of the transmitter diodes and the receiver chain, as well as to test and secure the exact pathway of the cable running from the receiver chain enclosure to the probe.

When performing ODNP measurements, the microwave resonance frequency of the cavity effectively fixes the NMR resonance frequency. (The cavity resonance, which typically cannot be adjusted, determines the B_0 field at which ESR resonance will be obtained, and therefore also determines the NMR frequency.) Therefore, it is important to achieve reasonable SNR even when the NMR resonance frequency happens to line up with one

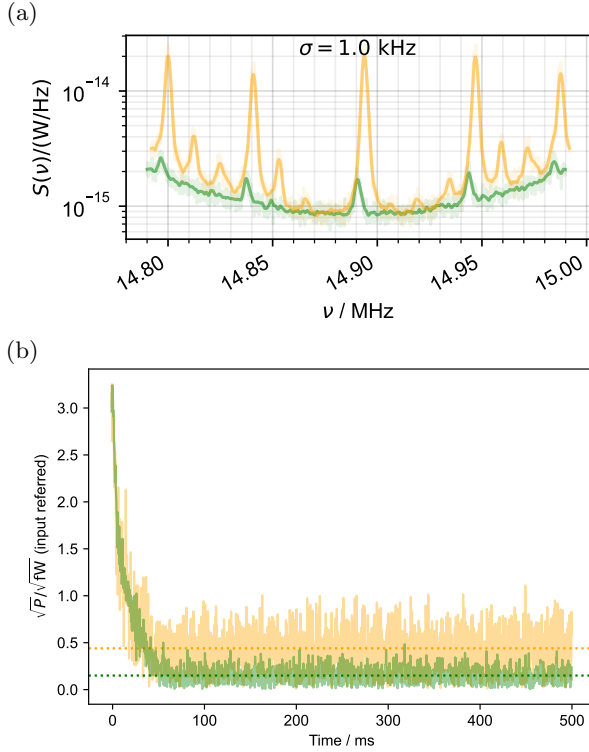


FIG. 15. (a): The noise PSD acquired with a 200kHz SW, without any form of mitigation (gold) rises magnitudes above the noise PSD acquired at a SW of 200 kHz with the toroid in place and ideal positioning of coax. cabling (green). (b): When an FID is acquired on resonance with the center spike in (a), the signal level remains consistent for both with and without mitigation techniques. However, the average noise power without the toroid (gold) is $0.44 \sqrt{fW}$ (input referred) illustrated by the dashed gold line while the average noise power with the toroid in place (green) is only $0.15 \sqrt{fW}$ (input referred) shown by the dashed green line.

of the EMI spikes (Fig. 15). [74]

Fig. 15 illustrates that the addition of rf chokes does not affect the overall amplitude of signal acquired on the NMR receiver and strictly acts to reduce noise, thus improving the overall SNR and sensitivity. Even though the SNR of the FID without chokes (gold in Fig. 15) seems reasonable, there is still a clear benefit of the inclusion of rf chokes by the further reduction of noise (green in Fig. 15). Unfortunately, there are situations in which the noise levels without mitigation strategies in place are much higher than those shown in Fig. 15, in which case the signal is barely recognizable (Sec. S1.7). These instances further emphasize the practical use of the presented protocol in finding the optimal mitigation techniques that are suitable for the given setup of the laboratory.

IV.3. Absolute signal intensity matches prediction

At this point, the noise has been characterized with a level of quantitative detail that allows one to test and select between different mitigation strategies. While at-

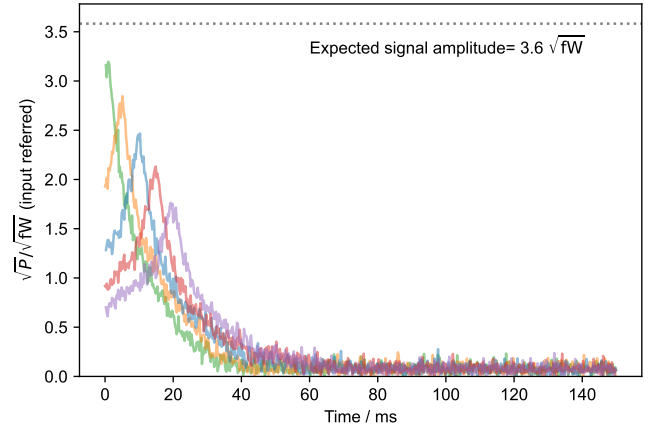


FIG. 16. An experiment with varied echo length performed on the same 27 mM TEMPOL sample. Signal comes from an echo sequence comprising a $\pi/2$ pulse, a delay τ that is varied for the differently colored signals, and a π pulse. A dashed black horizontal line indicates the predicted signal amplitude of $3.6 \sqrt{fW}$ (input referred).

tempts to improve the absolute ODNP signal amplitude will require the construction of new and involved hardware beyond the scope of this study, this section demonstrates the aforementioned adapted theory for predicting the absolute signal and breaking down the contributing factors to further improve the signal intensity.

Only the conversion factor, Λ , must be known to predict the absolute signal intensity (Eq. (7)). This involves a simple measurement of the power and pulse length required to yield a 90° pulse (Eq. (2)).

In the authors' lab, the rf amplifier outputs imperfect waveforms resulting in a pulse that is not a perfect rectangle and thus obfuscates this seemingly simple measurement. Therefore, it is necessary to calibrate the integral of $\sqrt{P_{tx}(t)}$ (see Eq. (S9)), and not possible (as is typical) to simply rely on an assumption of a rectangular pulse shape coupled with a single measurement of P_{tx} . Here, the $t_{90}\sqrt{P_{tx}}$ that generates optimal excitation is $17 \mu\text{s}\sqrt{W}$ (Sec. S1.9), corresponding to $\Lambda = 3.5 \times 10^2 \mu\text{T}/\sqrt{W}$ (Eq. (2)).

Based on this Λ value and a sample volume of $4.38 \mu\text{L}$, the predicted value for the square root of the signal power (input-referred) is $3.6 \sqrt{fW}$ (Eq. (7)). Experiments (Fig. 16) agree with this prediction fairly well. Specifically, Fig. 16 shows signal from a series of echoes with varying inter-pulse delays (τ) with the same averaging across the transients of the phase cycle that is applied to Fig. 15. The signal appears to extrapolate to the expected value ($3.6\sqrt{fW}$) at $\tau = 0$. Thus, a simple measurement of the $\pi/2$ pulse (in units of $\text{s}\sqrt{W}$), can determine the signal levels fairly accurately, as expected by the principle of reciprocity.

Having confirmed the ability of the theory to predict the absolute signal level, one can proceed to calculate the field distribution factor, η' , from Eq. (12). After a

(short-open-load) calibration, a nanoVNA (inexpensive pocket-sized VNA) measures the Q -factor of the probe to be 10.1. From this value, and the measured Λ , Eq. (12) determines a field distribution factor of $\eta' = 7.4 \times 10^{-3}$. This number, at first, seems unreasonably low. However, this result is not unreasonable if one considers the standard hairpin loop design employed in ODNP [1, 4, 6, 24]. The design consists of two loops of wire that are threaded parallel to the capillary tube, through two teflon spacers at opposite ends of the capillary tube. Measurements of the inductance of the hairpin loop coil (84 nH employing a resonant RLC circuit) reveal that the hairpin loop inductance is close to the theoretical inductance of a straight wire before winding into the hairpin loop structure. Therefore, the stored magnetic field energy of stray inductances compete with that of the coil. Specifically, the wires and circuit board within the tuning circuit and especially in the thin lead wires that lead from the tuning circuitry into the center of the cavity likely generate competing inductances. Furthermore, because the overwhelming majority of the stored magnetic field energy of a straight wire is stored very near to the wire, even with the wires relatively close to the sample, it is likely that a greater amount of magnetic field energy is stored near to the wires rather than in the volume containing the sample.

Fig. 17 presents a very basic calculation of the fields in the typical hairpin loop structure. Note that extended regions closer to the wires store $1.5-1.7\times$ as much energy as the field flowing through the sample (Fig. 17a). The field distribution factor calculated from Fig. 17a is 7% (according to Eq. (10)). Fig. 17b demonstrates that the mutual inductance of the wires does increase the field at the sample, but not as much as in other regions outside the sample. Also, because cancellation of the fields at the top and bottom leads to less energy storage, the finite inductance per unit length in this calculation (calculated from the 2D magnetic energy density per unit current integrated over a finite grid) is actually less than the sum of inductances achieved with one of the four wires active at a time. Therefore, this basic calculation supports at least one order of magnitude loss of the field distribution factor and, more importantly, supports the idea that the inductance of the hairpin loop is so low that it competes with single-wire inductances elsewhere in the tuning circuit.

As, by improving this surprising low value of η' , one could improve the signal amplitude by $40\times$, moving forward, one is motivated to pursue new ODNP probe designs that employ higher inductance coils to more effectively concentrate field into the sample. Admittedly, this strategy does present several challenges. In the past, the need to avoid perturbation of the microwave field inside the cavity was the primary driver for ODNP probe designs at X-band. However, by pointing to the fact that η' is orders of magnitude less than the Q -factor, the current study opens up new possibilities, such as resorting to very fine-gauge wire that might allow multiple loops

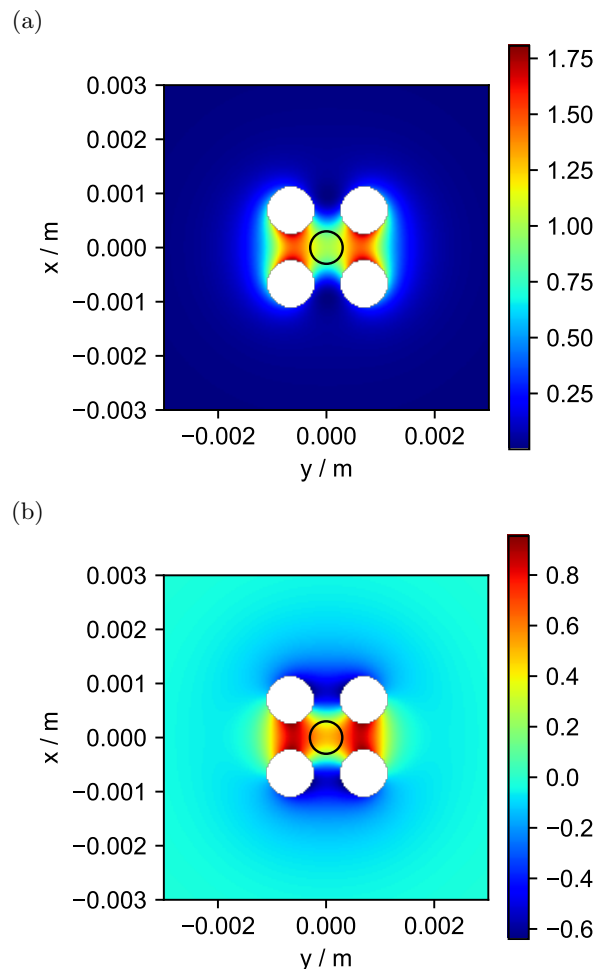


FIG. 17. A very simple simulation assuming infinite wires perpendicular to the page that generate a field of magnitude $\mu_0 I / 2\pi r$ (where r is the distance to the wire) and direction determined by Biot-Savart cross-product. The white circles indicate the location of the wires. (a): The magnetic field energy density normalized against the magnetic energy density due to the desired field (*i.e.* the plot shows $|B|^2 / 4B_{1,avg}^2$, where $2B_{1,avg}$ is the field in the lab frame). The black circle indicates the sample region (and the y -component of the field within the circle is averaged to determine $2B_{1,avg}$). (b): The same calculation, subtracted from the fields generated by the four wires, one at a time.

without perturbing the microwave field.

V. Conclusion

This article quantitatively explored the status quo of the absolute signal and absolute noise intensities in an ODNP instrument with a standard home-built NMR probe. A reproducible protocol shows how to reduce the noise density to its theoretical lower limit (the thermal noise limit), while a reorganization of the theory not only demonstrates a predictive understanding of the absolute signal level, but – for this case study of ODNP – identifies clear areas for future improvement of the SNR by up to $40\times$.

Open-source software, paired with very standard instrumentation and some limited data-processing, successfully enabled a detailed characterization of the absolute noise density, as well as a measurement of the response of the receiver. The protocol introduced here thus identified which new components were introduced to the noise density by the receiver, whether internally generated (high frequency) components, or aliasing arising from imperfections in the oversampling filters.

The general strategy outlined here could be adapted to any low-field system. The literature abounds with

interesting and novel designs, with many new and exciting opportunities for advanced and portable magnet systems, for customized spectrometer circuitry, and even for adapting open-source software and software-defined radio hardware to develop customized NMR transceivers [27, 75, 76]. The current paper enables better cross-pollination between such developments in different laboratories. With specific respect to ODNP development, it should facilitate more systematic deployment of ODNP at different fields and resonance frequencies, enabling a more comprehensive exploration of dynamics.

-
- [1] J. M. Franck and S. Han. “Overhauser Dynamic Nuclear Polarization for the Study of Hydration Dynamics, Explained.” In “Methods in Enzymology,” volume 615, pages 131–175. Elsevier (2019). ISBN 978-0-12-816762-5.
- [2] M. W. Berkow, H. Gwak, M. N. Idso, M. B. Schmithorst, B. E. Rhodes, B. D. Price, D. S. Gianola, S. Han, and B. F. Chmelka. “Co-Assembly of Functionally Active Proteorhodopsin Membrane Protein Molecules in Mesostructured Silica-Surfactant Films.” *Chemistry of Materials*, 35(20):8502–8516 (2023). doi:10.1021/acs/chemmater.3c01303.
- [3] J. H. Ortony, D. S. Hwang, J. M. Franck, J. H. Waite, and S. Han. “Asymmetric Collapse in Biomimetic Complex Coacervates Revealed by Local Polymer and Water Dynamics.” *Biomacromolecules*, 14(5):1395–1402 (2013). doi:10.1021/bm4000579.
- [4] B. D. Armstrong and S. Han. “Overhauser Dynamic Nuclear Polarization To Study Local Water Dynamics.” *Journal of the American Chemical Society*, 131(13):4641–4647 (2009). doi:10.1021/ja809259q.
- [5] A. A. Beaton, A. Guinness, and J. M. Franck. “A Modernized View of Coherence Pathways Applied to Magnetic Resonance Experiments in Unstable, Inhomogeneous Fields.” *The Journal of Chemical Physics*, 157(17):174204 (2022). doi:10.1063/5.0105388.
- [6] J. M. Franck, A. Pavlova, J. A. Scott, and S. Han. “Quantitative Cw Overhauser Effect Dynamic Nuclear Polarization for the Analysis of Local Water Dynamics.” *Progress in Nuclear Magnetic Resonance Spectroscopy*, 74:33–56 (2013). doi:10.1016/j.pnmrs.2013.06.001.
- [7] J. M. Franck, J. A. Scott, and S. Han. “Nonlinear Scaling of Surface Water Diffusion with Bulk Water Viscosity of Crowded Solutions.” *Journal of American Chemical Society*, 135(11) (2013). doi:10.1021/ja3112912.
- [8] K. M. Dunleavy, T. Li, E. Milshteyn, A. M. Jaufer, S. A. Walker, and G. E. Fanucci. “Charge Distribution Patterns of IA3 Impact Conformational Expansion and Hydration Diffusivity of the Disordered Ensemble.” *Journal of Physical Chemistry B*, 127(45) (2023). doi:10.1021/acs.jpcc.3c06170.
- [9] S.-B. Saun, J. Kim, R. Y. Hwang, Y. Ahn, D. Kim, D. K. Park, S. Lee, and O. H. Han. “Nanometer-Scale Water Dynamics in Nafion Polymer Electrolyte Membranes: Influence of Molecular Hydrophobicity and Water Content Revisited.” *ACS MacroLetters*, 9(7) (2020). doi:10.1021/acsmacrolett.0c00173.
- [10] A. Doll, E. Bordignon, B. Joseph, R. Tschaggelar, and G. Jeschke. “Liquid State DNP for Water Accessibility Measurements on Spin-Labeled Membrane Proteins at Physiological Temperatures.” *Journal of Magnetic Resonance*, 222:34–43 (2012). doi:10.1016/j.jmr.2012.06.003.
- [11] T. Uberruck, M. Adams, J. Granwehr, and B. Blumich. “A Compact X-Band ODNP Spectrometer towards Hyperpolarized 1H Spectroscopy.” *Journal of Magnetic Resonance (San Diego, Calif.: 1997)*, 314:106724 (2020). doi:10.1016/j.jmr.2020.106724.
- [12] T. J. Keller, A. J. Laut, J. Sirigiri, and T. Maly. “High-Resolution Overhauser Dynamic Nuclear Polarization Enhanced Proton NMR Spectroscopy at Low Magnetic Fields.” *Journal of Magnetic Resonance*, 313:106719 (2020). doi:10.1016/j.jmr.2020.106719.
- [13] B. Chaubey, A. Dey, A. Banerjee, N. Chandrakumar, and S. Pal. “Assessment of the Role of 2,2,2-Trifluoroethanol Solvent Dynamics in Inducing Conformational Transitions in Melittin: An Approach with Solvent 19F Low-Field NMR Relaxation and Overhauser Dynamic Nuclear Polarization Studies.” *Journal of Physical Chemistry B*, 124(28):5993–6003 (2020).
- [14] C. George and N. Chandrakumar. “Chemical-Shift-Resolved 19F NMR Spectroscopy between 13.5 and 135 MHz: Overhauser-DNP-Enhanced Diagonal Suppressed Correlation Spectroscopy.” *Angewandte Chemie International Edition*, 53(32):8441–8444 (2014). doi:10.1002/anie.201402320.
- [15] F. A. Perras, D. F. Flesariu, S. A. Southern, C. Nicolaides, J. D. Bazak, N. M. Washton, T. Trypiniotis, C. P. Constantinides, and P. A. Koutentis. “Methyl-Driven Overhauser Dynamic Nuclear Polarization.” *Journal of Physical Chemistry Letters*, 13:4000–4006 (2022). doi:10.1021/acs.jpcclett.2c00748.
- [16] A. Dey and A. Banerjee. “Unusual Overhauser Dynamic Nuclear Polarization Behavior of Fluorinated Alcohols at Room Temperature.” *The Journal of Physical Chemistry B*, 123(49):10463–10469 (2019). doi:10.1021/acs.jpcc.9b08144.
- [17] A. E. Marble, I. V. Mastikhin, B. G. Colpitts, and B. J. Balcom. “A Compact Permanent Magnet Array with a Remote Homogeneous Field.” *Journal of Magnetic Resonance*, 186(1):100–104 (2007). doi:10.1016/j.jmr.2007.01.020.
- [18] T. Kremer, T. Irons, M. Muller-Petke, and J. Juul Larsen. “Review of Acquisition and Signal Processing Methods for Electromagnetic Noise Reduction and Retrieval of Surface Nuclear Magnetic Resonance

- Parameters.” *Surveys in Geophysics*, 43(4):999–1053 (2022). doi:10.1007/s10712-022-09695-3.
- [19] R. Kleinberg. “NMR Well Logging at Schlumberger.” *Concepts in Magnetic Resonance*, 13:396–403 (2001). doi:10.1002/cmr.1026.
- [20] G. Jin, R. Xie, and B. Jin. “New Insight Into Data Processing of Nuclear Magnetic Resonance Logging for Pore Structure Characterization in Tight Sandstone Reservoirs.” *IEEE Transactions on Geoscience and Remote Sensing*, 62:1–10 (2024). doi:10.1109/TGRS.2024.3368096.
- [21] T. Lin, Y. Zhang, and M. Muller-Petke. “Random Noise Suppression of Magnetic Resonance Sounding Oscillating Signal by Combining Empirical Mode Decomposition and Time-Frequency Peak Filtering.” *IEEE access : practical innovations, open solutions*, 7:79917–79926 (2019). doi:10.1109/ACCESS.2019.2923689.
- [22] T. Lin, Y. Yang, F. Teng, and M. Muller-Petke. “Enabling Surface Nuclear Magnetic Resonance at High-Noise Environments Using a Pre-Polarization Pulse.” *Geophysical Journal International*, 212(2):1463–1467 (2018). doi:10.1093/gji/ggx490.
- [23] B. Blumich and J. Anders. “When the MOUSE Leaves the House.” *Magnetic Resonance*, 2(1):149–160 (2021). doi:10.5194/mr-2-149-2021.
- [24] I. Kaminker, R. Barnes, and S. Han. “Chapter Sixteen - Overhauser Dynamic Nuclear Polarization Studies on Local Water Dynamics.” In P. Z. Qin and K. Warncke, editors, “Methods in Enzymology,” volume 564 of *Electron Paramagnetic Resonance Investigations of Biological Systems by Using Spin Labels, Spin Probes, and Intrinsic Metal Ions, Part B*, pages 457–483. Academic Press (2015).
- [25] M. Teucher, S. Kucher, M. H. Timachi, C. B. Wilson, D. Smilowicz, R. Stoll, N. Metzler-Nolte, M. S. Sherwin, S. Han, and E. Bordignon. “Spectroscopically Orthogonal Spin Labels in Structural Biology at Physiological Temperatures.” *The Journal of Physical Chemistry B*, 127(30):6668–6674 (2023). doi:10.1021/acs.jpcc.3c04497.
- [26] D. M. Morin, S. Richard, N. Ansaribaranghar, B. Newling, and B. J. Balcom. “A Low-Field Ceramic Magnet Design for Magnetic Resonance.” *Journal of Magnetic Resonance*, 358:107599 (2024). doi:10.1016/j.jmr.2023.107599.
- [27] A. Doll. “Pulsed and Continuous-wave Magnetic Resonance Spectroscopy using a Low-Cost Software-defined Radio.” *AIP Advances*, 9:115110 (2019). doi:10.1063/1.5127746.
- [28] N. Hoepker, S. Lekkala, R. F. Loring, and J. A. Marohn. “Dielectric Fluctuations over Polymer Films Detected Using an Atomic Force Microscope.” *The Journal of Physical Chemistry B*, 115(49):14493–14500 (2011). doi:10.1021/jp207387d.
- [29] D. Fitzpatrick. “Chapter 14 - Noise Analysis.” In D. Fitzpatrick, editor, “Analog Design and Simulation Using OrCAD Capture and PSpice (Second Edition),” pages 197–208. Newnes (2018). ISBN 978-0-08-102505-5.
- [30] M. C. Boucher, C. E. Isaac, P. Sun, P. P. Borbat, and J. A. Marohn. “A Non-Perturbative, Low-Noise Surface Coating for Sensitive Force-Gradient Detection of Electron Spin Resonance in Thin Films.” *ACS Nano*, 17(2):1153–1165 (2023). doi:10.1021/acsnano.2c08635.
- [31] T. Hiller, R. Dlugosch, and M. Muller-Petke. “Utilizing Pre-Polarization to Enhance SNMR Signals—Effect of Imperfect Switch-Off.” *Geophysical Journal International*, 222(2):815–826 (2020). doi:10.1093/gji/ggaa216.
- [32] D. D. L. Chung. “Materials for Electromagnetic Interference Shielding.” *Materials Chemistry and Physics*, 255:123587 (2020). doi:10.1016/j.matchemphys.2020.123587.
- [33] V. Radeka. “Shielding and Grounding in Large Detectors.” Technical Report BNL-65912; CONF-980977-, Brookhaven National Lab. (BNL), Upton, NY (United States) (1998).
- [34] S. Sankaran, K. Deshmukh, M. B. Ahamed, and S. K. Khadheer Pasha. “Recent Advances in Electromagnetic Interference Shielding Properties of Metal and Carbon Filler Reinforced Flexible Polymer Composites: A Review.” *Composites Part A: Applied Science and Manufacturing*, 114:49–71 (2018). doi:10.1016/j.compositesa.2018.08.006.
- [35] P. Andris and I. Frollo. “Noise and Interference in Measured NMR Images.” *Measurement*, 77:29–33 (2016). doi:10.1016/j.measurement.2015.09.003.
- [36] L. Yang, W. He, Y. He, J. Wu, S. Shen, and Z. Xu. “Active EMI Suppression System for a 50 mT Unshielded Portable MRI Scanner.” *IEEE Transactions on Biomedical Engineering*, 69(11):3415–3426 (2022). doi:10.1109/TBME.2022.3170450.
- [37] P. Andris, E. F. Emery, and I. Frollo. “Analysis of NMR Spectrometer Receiver Noise Figure.” *Mathematical Problems in Engineering*, 2019:e1083706 (2019). doi:10.1155/2019/1083706.
- [38] P. Andris, V. Jacko, T. Dermek, and I. Frollo. “Noise Measurement of a Preamplifier with High Input Impedance Using an NMR Console.” *Measurement*, 55:408–412 (2014). doi:10.1016/j.measurement.2014.05.032.
- [39] J.-H. Ardenkjaer-Larsen, G. S. Boebinger, A. Comment, S. Duckett, A. S. Edison, F. Engelke, C. Griesinger, R. G. Griffin, C. Hilty, H. Maeda, G. Parigi, T. Prisner, E. Ravera, J. van Bentum, S. Vega, A. Webb, C. Luchinat, H. Schwalbe, and L. Frydman. “Facing and Overcoming Sensitivity Challenges in Biomolecular NMR Spectroscopy.” *Angewandte Chemie International Edition*, 54(32):9162–9185 (2015). doi:10.1002/anie.201410653.
- [40] M. Goryawala, M. Sullivan, and A. A. Maudsley. “Effects of Apodization Smoothing and Denoising on Spectral Fitting.” *Magnetic resonance imaging*, 70:108–114 (2020). doi:10.1016/j.mri.2020.04.013.
- [41] A. Ebel, W. Dreher, and D. Leibfritz. “Effects of Zero-Filling and Apodization on Spectral Integrals in Discrete Fourier-transform Spectroscopy of Noisy Data.” *Journal of Magnetic Resonance*, 182(2):330–338 (2006). doi:10.1016/j.jmr.2006.06.026.
- [42] D. D. Traficante and M. Rajabzadeh. “Optimum Window Function for Sensitivity Enhancement of NMR Signals.” *Concepts in Magnetic Resonance*, 12(2):83–101 (2000). doi:10.1002/(SICI)1099-0534(2000)12:2;83::AID-CMR3;3.0.CO;2-H.
- [43] R. R. Ernst and W. A. Anderson. “Application of Fourier Transform Spectroscopy to Magnetic Resonance.” *Review of Scientific Instruments*, 37(1):93–102 (2004). doi:10.1063/1.1719961.
- [44] J. Cavanagh, W. J. Fairbrother, A. G. Palmer, M. Rance, and N. J. Skelton. “Chapter 3 - Experimental Aspects of Nmr Spectroscopy.” In J. Cavanagh, W. J. Fairbrother, A. G. Palmer, M. Rance, and N. J. Skelton, editors, “Protein NMR Spectroscopy (Second Edition),” pages 107–

126. Academic Press, Burlington (2007). ISBN 978-0-12-164491-8.
- [45] D. I. Hoult and R. E. Richards. “The Signal-to-Noise Ratio of the Nuclear Magnetic Resonance Experiment.” *Journal of Magnetic Resonance* (1969), 24(1):71–85 (1976). doi:10.1016/0022-2364(76)90233-X.
- [46] W. Mims. “Electron Spin Echoes.” In “Electron Paramagnetic Resonance,” pages 263–351. S. Geschwind, ed. (1972).
- [47] R. R. Mett, J. W. Sidabras, I. S. Golovina, and J. S. Hyde. “Dielectric Microwave Resonators in TE₀₁₁ Cavities for Electron Paramagnetic Resonance Spectroscopy.” *The Review of Scientific Instruments*, 79(9):094702 (2008). doi:10.1063/1.2976033.
- [48] G. A. Rinard, R. W. Quine, S. S. Eaton, G. R. Eaton, and W. Froncisz. “Relative Benefits of Overcoupled Resonators vs Inherently Low-Q Resonators for Pulsed Magnetic Resonance.” *Journal of Magnetic Resonance, Series A*, 108(1):71–81 (1994). doi:10.1006/jmra.1994.1090.
- [49] O. Neudert, C. Mattea, and S. Stapf. “A compact X-Band resonator for DNP-enhanced Fast-Field-Cycling NMR.” *Journal of Magnetic Resonance*, 271 (2016). doi:10.1016/j.jmr.2016.08.002.
- [50] G. Annin, J. Villanueva-Garibay, P. van Bentum, A. Klaassen, and A. Kentgens. “A High-Conversion-Factor, Double-Resonance Structure for High-Field Dynamic Nuclear Polarization.” *Applied Magnetic Resonance*, 37(1):851 (2009). doi:10.1007/s00723-009-0091-6.
- [51] M. Conradi. “NMR Instrumentation - A Primer.” *Journal of Magnetic Resonance Open*, 12-13:100081 (2022). doi:10.1016/j.jmro.2022.100081.
- [52] Eq. (9) only assumes that the spins do not diffuse over the timescale of the experiment between regions with significantly different orientations of B_1 , so that any rf field perpendicular to B_0 excites spins in an equivalent fashion. Also note, the fields are only integrated over the sample volume.
- [53] H. Hill and R. E. Richards. “Limits of measurement in magnetic resonance.” *J. Phys. E: Sci. Instrum.*, 1(10) (1968). doi:10.1088/0022-3735/1/10/202.
- [54] N. Bloembergen, E. Purcell, and R. Pound. “Relaxation Effects in Nuclear Magnetic Resonance Absorption.” *Phys. Rev.*, 73(7):679–712 (1948). doi:10.1103/PhysRev.73.679.
- [55] N. Bloembergen. *Nuclear Magnetic Resonance*. Springer Dordrecht (1948). ISBN 978-94-017-5723-2.
- [56] H. Ladjouze and H. Benoit. “Filling factor for two-coil nuclear magnetic resonance spectrometer.” *Review of Scientific Instruments*, 44(12):1780–1781 (1973). doi:10.1063/1.1686054.
- [57] F. D. Doty. “Probe Design and Construction.” In “eMagRes,” John Wiley & Sons, Ltd (2015). ISBN 978-0-470-03459-0.
- [58] D. I. Hoult and R. E. Richards. “Critical factors in the design of sensitive high resolution nuclear magnetic resonance spectrometers.” *Proceedings of the Royal Society of London. A. Mathematical and Physical Sciences*, 344(1638):311–340 (1975). doi:10.1098/rspa.1975.0104.
- [59] G. A. Rinard, R. W. Quine, R. Song, G. R. Eaton, and S. S. Eaton. “Absolute EPR Spin Echo and Noise Intensities.” *Journal of Magnetic Resonance*, 140(1):69–83 (1999). doi:10.1006/jmre.1999.1823.
- [60] N. Bloembergen and R. V. Pound. “Radiation Damping in Magnetic Resonance Experiments.” *Phys. Rev.*, 95(1):8–12 (1954). doi:10.1103/PhysRev.95.8.
- [61] A. F. McDowell and N. L. Adolphi. “Operating Nanoliter Scale NMR Microcoils in a 1 Tesla Field.” *Journal of Magnetic Resonance*, 188(1):74–82 (2007). doi:10.1016/j.jmr.2007.06.008.
- [62] P. P. Borbat, R. H. Crepeau, and J. H. Freed. “Multifrequency Two-Dimensional Fourier Transform ESR: An X/Ku-Band Spectrometer.” *Journal of Magnetic Resonance*, 127(2):155–167 (1997). doi:10.1006/jmre.1997.1201.
- [63] Z. Ali, D. P. Poenar, and S. Aditya. “Design of Planar Microcoil-Based NMR Probe Ensuring High SNR.” *AIP Advances*, 7(9):095107 (2017). doi:10.1063/1.5002721.
- [64] A. Abragam. *The Principles of Nuclear Magnetism*. Clarendon Press, Oxford University (1961).
- [65] H. Nyquist. “Thermal Agitation of Electric Charge in Conductors.” *Physical Review*, 32(1):110–113 (1928). doi:10.1103/PhysRev.32.110.
- [66] H. Friis. “Noise Figures of Radio Receivers.” *Proceedings of the IRE*, 32(7):419–422 (1944). doi:10.1109/JRPROC.1944.232049.
- [67] D. J. Jiang and D. R. T. Weber. “Elexsys E 500 User’s Manual: Basic Operations.”
- [68] J. Franck, A. A. Beaton, and A. Guinness. “Instrument notebook.” <https://github.com/jmfrancklab/FLinst> (2017).
- [69] D. K. Rytting. “Network Analyzer Accuracy Overview.” In “58th ARFTG Conference Digest,” volume 40, pages 1–13 (2001).
- [70] J. A. Nordmeyer-Massner, N. De Zanche, and K. P. Pruessmann. “Noise Figure Characterization of Preamplifiers at NMR Frequencies.” *Journal of Magnetic Resonance*, 210(1):7–15 (2011). doi:10.1016/j.jmr.2011.01.025.
- [71] D. Micheli, R. Pastore, A. Vricella, A. Delfini, M. Marchetti, and F. Santoni. “Chapter 9 - Electromagnetic Characterization of Materials by Vector Network Analyzer Experimental Setup.” In S. Thomas, R. Thomas, A. K. Zachariah, and R. K. Mishra, editors, “Spectroscopic Methods for Nanomaterials Characterization,” Micro and Nano Technologies, pages 195–236. Elsevier (2017). ISBN 978-0-323-46140-5.
- [72] J. Mispelter, M. Lupu, and A. Briguet. *NMR Probeheads for Biophysical and Biomedical Experiments: Theoretical Principles and Practical Guidelines (With CD-ROM)*. Imperial College Press and World Scientific Publishing co. (2006). ISBN 978-1-86094-637-0 978-1-86094-902-9.
- [73] J. Stringer and B. F. Collins. “(54) Balanced Mode Operation of a High Frequency NMR Probe.” (2).
- [74] The signal has been averaged across the transients of the four step phase cycle in Fig. 15, so that the displayed signal amplitude equals that of a single transient, while the noise amplitude is $1/\sqrt{4}$ the noise amplitude of a single transient.
- [75] C. A. Michal. “A low-cost multi-channel software-defined radio-based NMR spectrometer and ultra-affordable digital pulse programmer.” *Concepts in Magnetic Resonance Part B: Magnetic Resonance Engineering*, 48B(3):e21401 (2018). doi:10.1002/cmr.b.21401.
- [76] D. D. Griffin, R. L. Kleinberg, and M. Fukuhara. “Low-Frequency NMR Spectrometer.” *Measurement Science and Technology*, 4(9):968 (1993). doi:10.1088/0957-0233/4/9/009.

Supplemental Materials for: Separate and Detailed Characterization of Signal and Noise Enables NMR Under Adverse Circumstances

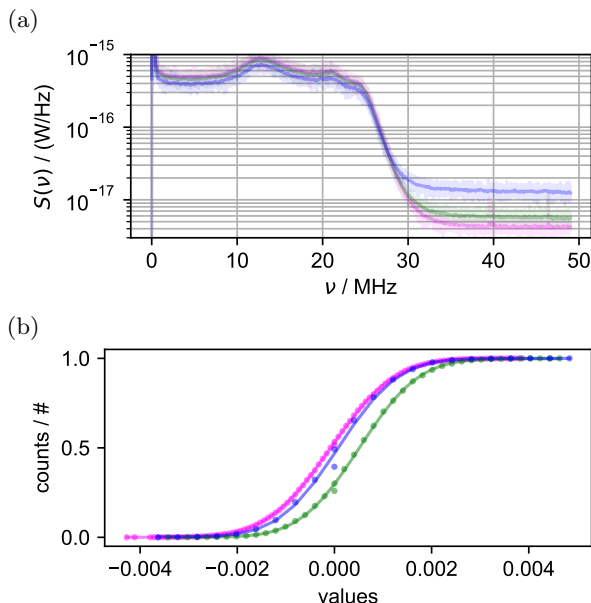


FIG. S1. (a): PSD of the terminated receiver chain acquired on the oscilloscope with a voltscale of 2 (magenta), 5 (green) and 10 (blue) mV. Here the y axis of the plot is zoomed to emphasize the difference in PSD. (b): The normalized gaussian cumulant of each measurement fit with a spline, plotted using the same colors as A.

S1. Supporting Information

S1.1. Broadband Noise PSD Summary

The problem of DC power supplies acting as noise sources for ODNP is not a new observation, and various individual solutions have been implemented, frequently at the expense of great experimental time, but the same solutions do not apply to every unique setup in each laboratory [S1]. The overarching observation here is that performing a noise PSD measurement of reasonable quality allows one to: (1) identify primary sources of noise (2) systematically identify which solutions help to mitigate those noise sources and which do not, and (3) identify how closely a particular noise density comes to the idealized thermal (Johnson-Nyquist) noise limit (*vs.* how much interference noise or poor noise figures dominate the noise spectrum).

Importantly, the measured noise PSDs are expected to be idiosyncratic for the particular laboratory setup where these measurements were acquired; it is the measurement protocol itself rather than the particular data that is expected to prove transferable to other laboratories and types of experiments.

S1.2. Digitization Rates of Oscilloscope

The voltscale setting of the oscilloscope dictates the vertical scale of acquisition. Depending on the setting,

| Spectral width (kHz) | Receiver Calibration (dg / μ V) |
|----------------------|-------------------------------------|
| 4 | 476.4 |
| 40 | 727.8 |
| 200 | 583.0 |
| 1000 | 466.0 |
| 4000 | 117.7 |
| 10000 | 49.73 |
| 75000 | 6.054 |

TABLE I. The appropriate receiver calibration factor in units of dg/ μ V, acquired by measuring the ratio between the raw digitizer units and the voltage amplitude of the ≈ 15 MHz sine wave (≈ 15 mV) injected into receiver. Amplitudes determined from the fit of the captured sine wave, and significant figures reflect variance of five measurements. These values were later validated by plotting the response function of the digital filter of the SpinCore divided by the output voltage as acquired on the oscilloscope (Sec. IV.2.C).

the resulting PSD for the noise before the low pass filter threshold may appear lower in power than actuality, while the PSD for the noise after the threshold may appear higher (e.g. the blue line in Fig. S1a). This was investigated by analyzing the Gaussian cumulant of unique datasets with varying voltage settings (Fig. S1b). Notably, the Gaussian cumulant of the larger voltscales (the blue and green lines) are much wider and include a jump for values about 0. Whereas the Gaussian cumulant for the 2 mV (smallest voltscale setting on the GDS) demonstrates a typical Gaussian noise distribution and is relatively smooth transitioning from lower values to higher values. When comparing the broadband noise PSDs to the narrow noise PSDs acquired on the receiver board, this is an important note to take into consideration as the two PSDs will inadvertently show a mismatch in power if the broadband measurements are acquired with a larger voltscale.

S1.3. Receiver Calibration Factor

The AFG injected $1 V_{amp}$ into 2 calibrated attenuation assemblies followed by the receiver chain to generate a final test signal with a voltage of 15.21 mV and a frequency of 15 MHz, which was verified first by acquiring on the oscilloscope. The SpinCore transceiver board then acquired the test signal at the set spectral widths (in the case of Fig. S2 - 200kHz) with four transients. The amplitude in digunits, is obtained by fitting each complex transient to Euler's formula and taking the average of the fit amplitudes. The final receiver calibration factor is determined by taking the ratio of the averaged amplitudes ([digunits]) to the real voltage value of the injected test signal ([V], measured by the oscilloscope).

The values of Table I were later validated by tracing the response function of the SpinCore's digital filter using

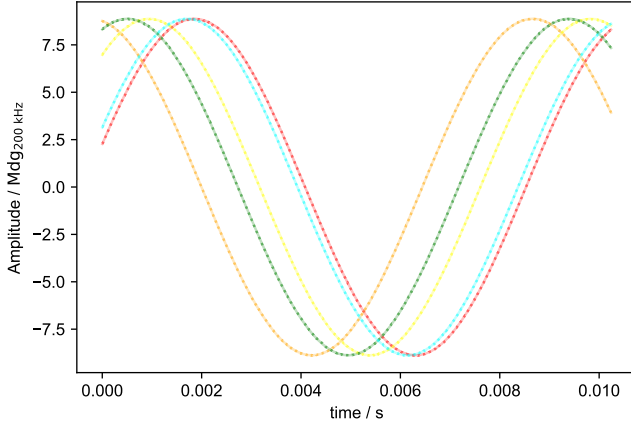


FIG. S2. Test signal with a voltage amplitude of 15.21 mV is injected into the SpinCore transceiver board and 4 transients are acquired using a spectral width of 200 kHz. Each complex transient is fit to Euler's formula to extract an amplitude of 8.876×10^6 dg in arbitrary digitizer-specific units [dg] assigned by the transceiver board.

the AFG source which output a sine wave with an amplitude of 5 mV at a range of frequencies that spanned 2X the spectral width of the SpinCore data (Sec. S1.11.B). Each frequency acquired was averaged 25 times and the max of the noise PSD was plotted as a function of offset from the carrier frequency. The resulting curve was then divided by the PSD for each respective output frequency as acquired on the oscilloscope. The max of the square root of the curve (corresponding to 0 offset from the carrier) produces the final transceiver calibration factor for the respective spectral width (dg/ μ V). These values match well with the factors found when fitting the time domain captures of the 15.21 mV test signal to a complex wave function.

S1.4. High-frequency Noise of Transceiver

After observing the higher frequency oscillations in Fig. 9, the PSD was further investigated by varying the attenuation between the output of the receiver chain and the input of the transceiver board (Fig. S3) and acquiring at a spectral width of 75 MHz. This verifies that the noise does scale with the input and supports the idea that these oscillating peaks arise from the receiver board itself.

S1.5. Predicting wide spectral width PSD

The spectral widths with predictions are acquired and decreased step-wise until a spectral width of 3.9 kHz is eventually reached (figure S4). As stated previously this noise peak appears to be a standalone spike at this spectral width. Had the wider spectral width PSDs not been taken one might not realize that this peak arises from through space EMI or how to mitigate the effect to isolate the desired signal at this zoomed in spectral width.

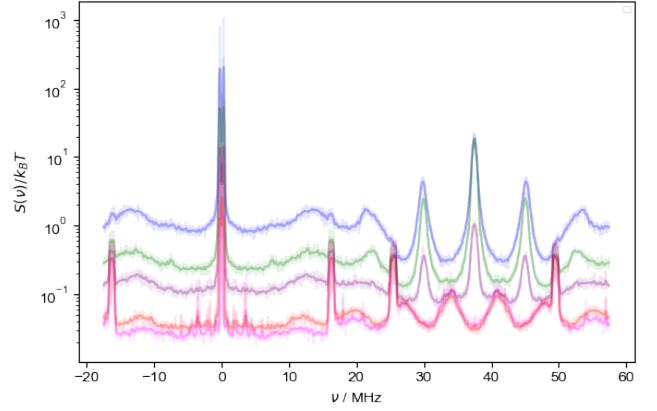


FIG. S3. A variable attenuator placed between the output of the terminated receiver chain and the input of the SpinCore generated attenuations of 3 dB (blue), 10 dB (green), 13 dB (purple), and 23 dB (red). The terminated SpinCore (magenta) served as a reference. Both the noise and high frequency harmonics scale with attenuation up to 13 dB. At 23 dB the oscillations shift frequency and resemble the terminated SpinCore PSD in Fig. 9.

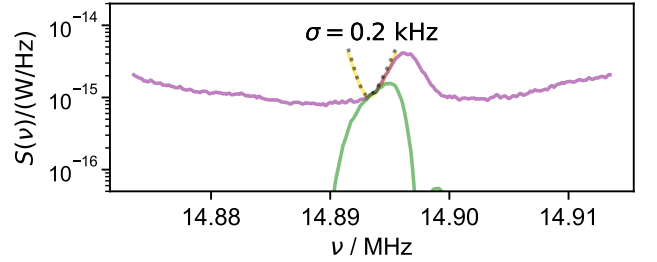


FIG. S4. The PSD acquired on the transceiver board using $SW = 40$ kHz is divided by a sinc function appropriate for a spectral width of 40 kHz (purple) and subsequently multiplied by a narrower sinc function appropriate for a dataset with a spectral width of 3.9 kHz to yield a filtered noise PSD (green). The downsampling of this product produces the predicted noise PSD for a spectrum taken with a spectral width of 3.9 kHz (dashed black line). The actual acquired spectra (gold) having a spectral width of 3.9 kHz shows the exact same PSD as the predicted model.

S1.6. Quantification of Gain

The gain of the receiver pathway was calculated by outputting a measured test signal over a range of rf frequencies into the receiver pathway and the amplified noise was collected on the oscilloscope (Fig. S5, acquired with a variation of Sec. S1.11.B).

The plot of measured test signal indicates a fairly consistent amplitude output of the AFG (Fig. S5a), while the output power of the receiver chain (Fig. S5b) shows a clear rise in power at a frequency of 12.5 MHz. The ratio of the output power of the receiver chain to the output power of the AFG produces the final calculation of the

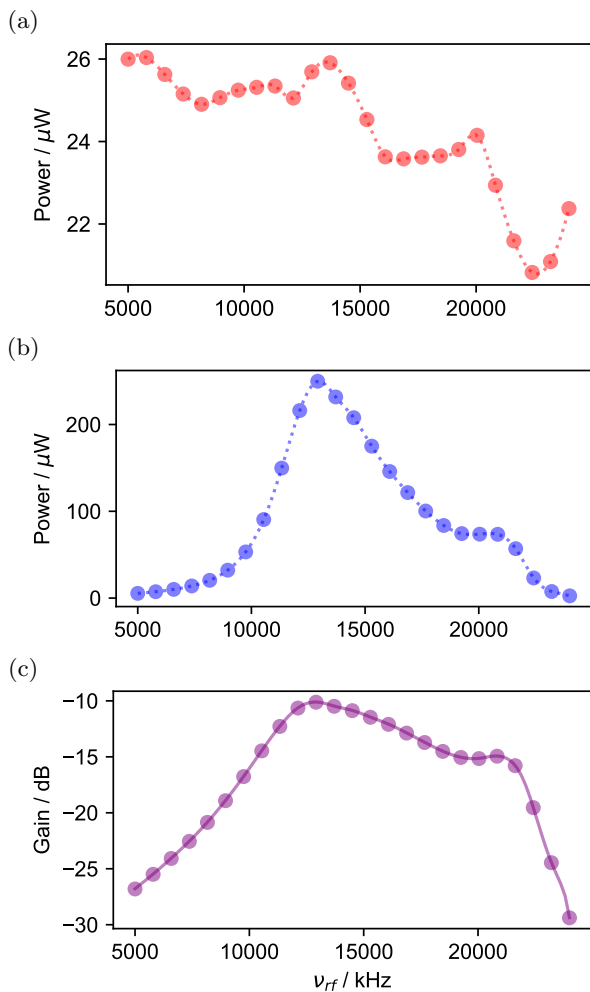


FIG. S5. (a): The AFG outputs test signal output directly to the oscilloscope and the acquired power as a function of frequencies is fit to a cubic spline. (b): The test signal from (a) is injected into a 40.021 dB attenuator assembly prior to the input of the receiver chain. The oscilloscope captures the amplified test signal at the output of the receiver chain and is plotted as a function of the frequencies. (c): Gain in dB calculated with the attenuator taken into consideration, as a function of the input frequency.

gain as a function of frequencies (Fig. S5c). This trend in gain variation is most likely due to the analog components of the receiver chain (e.g., the included pi circuits and tuned limiter) acting as additional filters. This measurement is key to properly quantifying the signal and noise in later steps to calculate the input-referred signal.

S1.7. Cases of Extreme Noise

In a given ODNP experiment, the user often does not have control over which NMR frequency to tune to (since it is largely determined by the cavity resonance which typically cannot be adjusted). This puts the user in an unfortunate situation when that frequency lays on an intense noise spike. In extreme cases of noise the signal is buried in the noise and may not even be noticeable to the

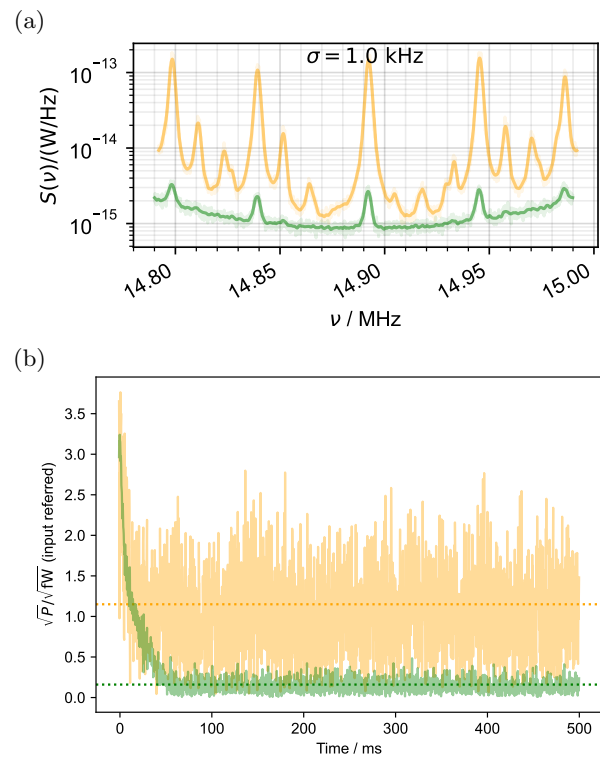


FIG. S6. (a): The noise PSD acquired with a SW of 200 kHz, without any form of mitigation (gold) rises magnitudes above the noise PSD acquired when optimal cable positioning and a ferrite toroid is in place (green). (b): When the signal is acquired on the central spike, with no form of mitigation techniques (gold) the average power of the noise is $1.15 \sqrt{\text{fW}}$ (input referred, gold dashed line) obfuscating the $3.3 \sqrt{\text{fW}}$ of signal. When the toroid and optimal positioning of BNC cabling is used (green) and again the signal is acquired on the central spike, the noise level is reduced to $0.16 \sqrt{\text{fW}}$ (input referred, green dashed line) and the signal is clearly defined.

untrained eye (Fig. S6b). Use of a toroidal ferrite choke and noise PSDs (Fig. S6a) to find the ideal positioning of cables yields a ten-fold decrease in the noise so that the signal clearly rises above the noise levels in the FID.

S1.8. Deriving the Principle of Reciprocity

AG: this portion will need revision and relates to this slack convo: here Faraday's law forms the basis for the calculation of the produced emf in the receiving coil via:

$$\xi_{NMR} = \frac{d\Phi_{rcvg\ coil}}{dt} \quad (\text{S1})$$

where $\Phi_{rcvg\ coil}$ is the magnetic flux of the receiving coil. Note this is the induced emf from the magnetic moment of the spins within the sample. For the purposes of this derivation, we replace the spins by a current loop (Fig. S7) and the total sample magnetic moment is:

$$m_{spins} = I_{spins} A_{spins} \quad (\text{S2})$$

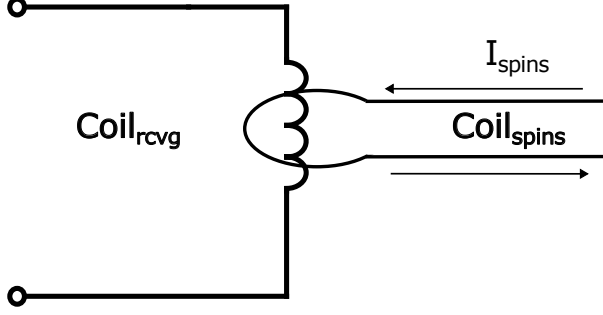


FIG. S7. Simple diagram of a NMR receiving coil (left) interacting with a current loop representing the spins of the sample that have magnetic moment m_{spins} (right).

where I_{spins} is the current in the current loop representing the spins, and A_{spins} can be considered the area of the current loop.

Eq. (S1) however, introduces a problem: the $\Phi_{rcvg\ coil}$ is an unknown. Fortunately, we can solve for it by inciting the law of mutual inductances:

$$\mathcal{M}_{rcvg\ coil, spins} = \mathcal{M}_{spins, rcvg\ coil} \quad (\text{S3})$$

where the magnetic flux of the coil induced by the current flowing through the current loop, $\mathcal{M}_{rcvg\ coil, spins} = \frac{\Phi_{rcvg\ coil}}{I_{spins}}$ is equal to the magnetic flux of the current loop induced by the current flowing through the receiving coil, $\mathcal{M}_{spins, rcvg\ coil} = \frac{\Phi_{spins}}{I_{rcvg\ coil}}$. In short, the magnetic flux of one coil is induced by the field produced by the other coil's current.

Furthermore, by expanding Φ_{spins} we can show

$$\mathcal{M}_{spins, rcvg\ coil} = \frac{A_{spins} B_{at\ spins}}{I_{coil}} \quad (\text{S4})$$

where $B_{at\ spins}$ is the field at the sample. Substituting $\mathcal{M}_{rcvg\ coil, spins} = \frac{\Phi_{rcvg\ coil}}{I_{spins}}$ into Eq. (S1) we get:

$$\xi_{NMR} = \omega \mathcal{M}_{rcvg\ coil, spins} I_{spins} \quad (\text{S5})$$

Due to the law of mutual inductances (Eq. (S3)), we replace $\mathcal{M}_{rcvg\ coil, spins}$ with $\mathcal{M}_{spins, rcvg\ coil}$. Combining this with Eq. (S4) and Eq. (S2), Eq. (S5) simplifies to:

$$\begin{aligned} \xi_{NMR} &= \omega \mathcal{M}_{spins, rcvg\ coil} I_{spins} \\ &= \omega \left(\frac{B_{at\ spins}}{I} \right) \left(\frac{m_{spins}}{A_{spins}} \right) \\ &= \omega \left(\frac{B_{at\ spins}}{I} \right) m_{spins} \end{aligned} \quad (\text{S6})$$

Thus, we show that the field generated at the spins is directly related to the produced emf (the principle of reciprocity).

Alternatively, we can start with the integral form of Faraday's law:

$$\xi(\mathbf{r}, \mathbf{t}) \approx -\frac{1}{4\pi} \iiint_V \frac{\left(\frac{\partial \mathbf{B}(\mathbf{r}', t)}{\partial t} \right) \times (\mathbf{r} - \mathbf{r}')}{|\mathbf{r} - \mathbf{r}'|^3} d^3 \mathbf{r}', \quad (\text{S7})$$

where $B(\mathbf{r}', t)$ is the magnetic field at position \mathbf{r}' as a function of time. It is not hard to recognize that this equation largely resembles Biot-Savart's integral form:

$$\mathbf{B}(\mathbf{r}) = \frac{\mu_0}{4\pi} \int \mathbf{J}(\mathbf{r}') \times \frac{\mathbf{r} - \mathbf{r}'}{|\mathbf{r} - \mathbf{r}'|^3} d^3 \mathbf{r}', \quad (\text{S8})$$

where $\mathbf{J}(\mathbf{r}')$ is the current density produced by a current flowing through the wire, and $\mathbf{r} - \mathbf{r}'$ is the vector between the wire/current and the location of field. If we assume that Biot-Savart's law can be transformed to a time dependent field (e.g. $\mathbf{B}(\mathbf{r}', t) = \mathbf{B}_1(\mathbf{r}') \cos(\omega t)$) and plug Eq. (S8) into Eq. (S7) we find a general proof of reciprocity relating the current induced by a magnetic field to the induced emf.

S1.9. Nutation Curve (Measurement of Λ)

The text notes (Sec. IV.3), that because the output pulse from the amplifier has a finite rise time and an imperfect shape in the authors' lab (Fig. S8c), it is necessary to calibrate the integral of $\sqrt{P_{tx}(t)}$, rather than simply relying on an assumption of a rectangular pulse shape coupled with a single measurement of P_{tx} (as is typical). For calibration, the oscilloscope captures pulses of varying pulse lengths output from the rf amplifier (attenuated with a calibrated attenuator). Each captured pulse is converted to analytic signal (Eq. (19)) and the average power calculated via Eq. (21). The final $t_{pulse} \sqrt{P_{tx}}$ is calculated via:

$$t_{pulse} \sqrt{P_{tx}} \equiv \frac{1}{\sqrt{50}} \int \frac{1}{\sqrt{2}} |s_a(t)| dt. \quad (\text{S9})$$

where t_{pulse} is the length of the output pulse and 50 is the resistance in Ω . To assist in this calculation a lorentzian filter with a width appropriate for the measured Q value is applied prior to integration. The $t_{pulse} \sqrt{P_{tx}}$ vs output pulse length is fit to a polynomial so that the desired $t_{90} \sqrt{P_{tx}}$ is obtained by extrapolating the proper pulse length from the calibration curve.

Armed with this calibration table, a simple nutation experiment can then employ linearly spaced $t_{pulse} \sqrt{P_{tx}}$ values. Fig. S8a shows the raw data of the nutation experiment as a domain colored coherence transfer pathway plot that illustrates a clear inversion from red to blue (indicating the $t_{180} \sqrt{P_{tx, rms}}$) at around $34 \mu s \sqrt{W}$. This data is integrated along the time axis to yield Fig. S8b verifying the optimal (90° tip) $t_{90} \sqrt{P_{tx}}$ at $17 \mu s \sqrt{W}$.

S1.10. Probe Circuit Diagrams

In addition to building the 'single-sided' probe containing the traditional tank circuit used for most NMR probes, we also constructed a second balanced probe with the aim of concentrating the current within the circuit

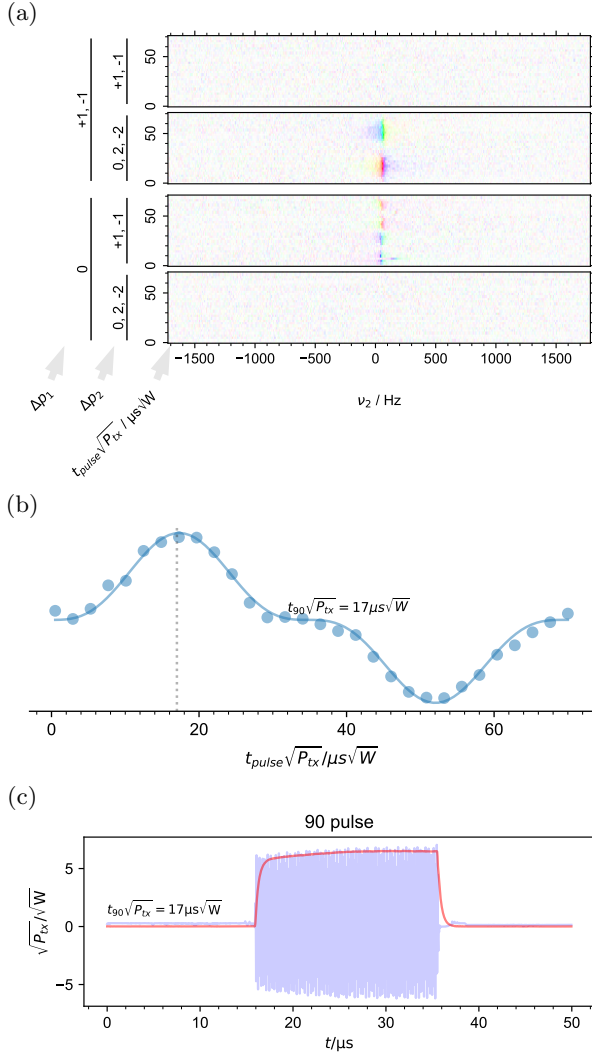


FIG. S8. (a): The domain colored coherence transfer pathway (DCCT) of the nutation experiment performed by varying the output $t_{90} \sqrt{P_{\text{tx}}}$ using a two step phase cycle on the 90° pulse and a two step phase cycle on the 180° pulse. The color change in $\Delta p_1 = +1, \Delta p_2 = -2$ indicates a rise in signal (yellow/red) followed by a null and finally an inversion to blue at longer pulse times. A color wheel is depicted for reference of phase. (b): The data is integrated to extrapolate the first maximum, indicative of a proper 90° tip at $17 \mu\text{s}\sqrt{\text{W}}$. (c): Capture of the 90° pulse on the oscilloscope. The analytic signal (blue) is frequency filtered using a lorentzian whose full width half-maximum is determined by measurement of $S_{1,1}$ on a network analyzer (red). Integration of the filtered pulse shows that the actual integral of the pulse ($t_{90} \sqrt{P_{\text{tx}}}$) as seen on the oscilloscope.

near the coil. [S2] explains that this design has the advantage of mitigating the antenna effect by almost equalizing the impedance to ground on either end of the coil. Both circuits are shown in Fig. S9. All parts used to build the circuits were purchased from DigiKey and minicircuits. The balanced probe was also built to accommodate shim coils between the magnets shown in Fig. 2 and therefore

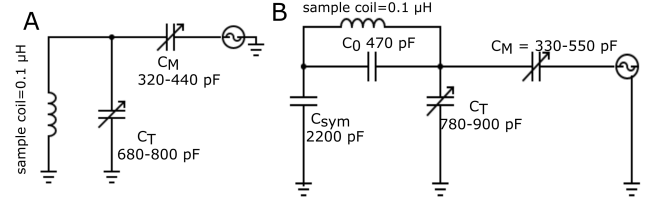


FIG. S9. Comparison of the two probe circuits. A) The “single sided” tank circuit consists of a tuning capacitance (C_T) and matching capacitance (C_M). Both include 120 pF variable capacitors in order to span a range of frequencies. The double hairpin coils for both probes have a volume of $8.55 \mu\text{L}$ and an inductance of $\sim 0.1 \mu\text{H}$ measured with a miniVNA. B) The circuitry used for the balanced probe includes two additional capacitors.

the tuning box containing the circuit is both slimmer and the frame itself is thinner compared to the single-sided probe. Therefore, while the balanced probe bears advantages in circuitry, the single-sided probe bears the advantage of a thicker encasement and therefore better shielding.

S1.11. Acquisition Scripts

When utilizing the oscilloscope, the instrument itself takes raw RS232 commands that utilize `write`. All other commands, properties and attributes were made in-house using [S3]. In the stage of calibrating the test signal, the oscilloscope captures a single capture of the waveform which is converted to the analytic and a rough frequency filter is applied to display the actual voltage amplitude using the following script:

```

from Instruments import GDS_scope
from pyspecdata import figlist_var
from matplotlib.pyplot import text, gca

expected_Vamp = 15e-3
filter_width_Hz = 10e6 # 10 MHz filter about the average
# frequency
with figlist_var() as fl:
    with GDS_scope() as g:
        g.reset()
        # {{ display settings - use channel 2
        g.CH1.disp = False
        g.CH2.disp = True
        g.CH3.disp = False
        # }}
        # {{ voltage scale and acquisition settings
        g.CH2.voltscal = (
            expected_Vamp * 1.1 / 4
        ) # set to a little more than  $\frac{V_{amp}}{4}$ 
        g.timscale(10e-9, pos=0)
        g.write(":TIM:MOD WIND")
        g.write(
            ":CHAN2:IMP 5.0E+1"
        ) # set impedance to 50 ohms
        g.write(
            ":TRIG:SOUR CH2"
        ) # set the source of the trigger to channel 2
        g.write(
            ":TRIG:MOD AUTO"
        ) # set trigger to auto

```



```

g.write(":ACQ:MOD HIR") # high vertical res.
# }}}
# {{{ set horizontal cursors on oscilloscope display
g.write(
    ":CURS:MOD HV"
) # set horizontal cursors
g.write(
    ":CURS:SOUR CH2"
) # cursors pertain to channel 2
# }}}
# {{{ use expected amplitude to set initial
# position of cursors
g.write(
    ":CURS:V1P "
    + ("%0.2e" % expected_Vamp).replace(
        "e", "E"
    )
)
g.write(
    ":CURS:V2P "
    + ("%0.2e" % -expected_Vamp).replace(
        "e", "E"
    )
)
# }}}
# {{{ grab waveform from oscilloscope
g.write(":SING") # capture single acquisition
data = g.waveform(ch=2)
assert data.get_units("t") == "s"
# }}}
fl.next("Signal captured on GDS oscilloscope")
fl.plot(data, label="raw signal")
# {{{ convert to analytic signal
data.ft("t", shift=True)
data = data["t"]:(0, None)
data *= 2
data["t", 0] *= 0.5
data.ift("t")
# }}}
fl.plot(abs(data), label="analytic signal")
frq = (
    data.C.phdiff("t", return_error=False)
    .mean("t")
    .item()
) # calculate average frequency of signal
# {{{ now, filter the signal about the average
data.ft("t")
data["t" : (0, frq - filter_width_Hz / 2)] = 0
data["t" : (frq + filter_width_Hz / 2, None)] = 0
data.ift("t")
# }}}
fl.plot(data, label="filtered analytic signal")
fl.plot(
    abs(data),
    label="filtered analytic signal",
)
Vamp = (
    abs(data["t"]:(1e-6, 4e-6))
    .mean("t")
    .real.item()
)
text(
    0.5,
    0.05,
    s="$V_{amp} = %0.6f$ mV" % (Vamp / 1e-3),
    transform=gca().transAxes,
)

```

S1.11.A. Capturing Noise Density

In order to adequately capture the noise density on the oscilloscope, the user must first manually adjust the desired settings (voltscale, sampling rate, and trigger) on the oscilloscope interface. The actual acquisition of the repeated captures is then acquired using the following script:

```

from datetime import datetime
from Instruments import GDS_scope
import sys
from pyspecdata import getDATADIR
from numpy import float64
import time

# {{{ Function for acquiring data
def collect(file_string, N_capture):
    with GDS_scope() as g:
        for x in range(N_capture):
            data = g.waveform(
                ch=2
            ) # take the waveform from channel 2
            if x == 0:
                s = (
                    data.shape + ("capture", N_capture)
                ).alloc(
                    dtype=float64
                ) # allocate an array that's shaped
                # like a single capture,
                # but with an additional "capture"
                # dimension
                s["t"] = data.getaxis("t")
                s.set_units("t", data.get_units("t"))
            s[
                "capture", x
            ] = data # store data for the capture in
                # the appropriate index
            time.sleep(1)
        s.setaxis(
            "capture", "#"
        ) # just set to a series of integers
        date = datetime.now().strftime("%y%m%d")
        s.name(
            "accumulated_" + date
        ) # nodename for h5 file
        s.hdf5_write(
            date + "_" + file_string + ".h5",
            directory=getDATADIR( # store in a directory
                # known to pyspecdata so
                # that storage location
                # doesn't depend on file
                # structure of computer it
                # is run on
                exp_type="ODNP_NMR_comp/noise_tests"
            ),
        )
    return

# }}}
def raise_arg_error():
    raise ValueError(
        """call like this:

```

```

python collect_GDS.py file_string N_capture
(where file_string is added to the filename
along with the date, and N_capture is the
number of captures you want to acquire)

```

```

        """
    )

if __name__ == "__main__":
    if len(sys.argv) < 3:
        raise_arg_error()
    file_string, N_capture = sys.argv[
        1:3
    ] # the filename will be the date followed by the
    # first argument in the terminal
    try:
        N_capture = int(N_capture)
    except:
        raise_arg_error()
    collect(
        file_string, int(N_capture)
    ) # acquire the data

```

Unlike the oscilloscope the SpinCore has no need for manual set up and simply requires the user to input the number of averages, spectral width and carrier into the following script before running:

```

import pyspecdata as ps
import numpy as np
from numpy import r_
import SpinCore_pp as sc
from datetime import datetime

# {{{ set filename, spectral width and carrier
date = datetime.now().strftime("%y%m%d")
description = "SpinCore_noise"
SW_kHz = 75000
output_name = (date + "_" + description + "_"
    + str(SW_kHz) + "kHz")
carrierFreq_MHz = 20
# }}}
# {{{ SpinCore settings
adcOffset = 38
tx_phases = r_[0.0, 90.0, 180.0, 270.0]
nScans = 100
nPoints = 1024 * 2
# }}}
# {{{ Acquire data
for x in range(nScans):
    # {{{ configure SpinCore
    sc.configureTX(
        adcOffset,
        carrierFreq_MHz,
        tx_phases,
        1.0,
        nPoints,
    )
    acq_time_ms = sc.configureRX(
        SW_kHz,
        nPoints,
        1,
        1, # assume nEchoes = 1
        1, # assume nPhaseSteps = 1
    )
    sc.init_ppg()
    # }}}
    # {{{ ppg to generate the SpinCore data
    sc.load(
        [
            ("marker", "start", 1),
            ("phase_reset", 1),

```

```

            ("delay", 0.5e3), # pick short delay (ms)
            ("acquire", acq_time_ms),
            ("delay", 1e4), # short rep_delay_us
            ("jumpto", "start"),
        ]
    )
    # }}}
    sc.stop_ppg()
    sc.runBoard()
    raw_data = ( # grab data for the single
        # capture as a complex value
        sc.getData(
            (2 * nPoints * 1 * 1),
            nPoints,
            1,
            1
        )
        .astype(float)
        .view(complex)
    ) # assume nEchoes and nPhaseSteps = 1
    # }}}
    # {{{ If this is the first scan, then allocate an
    # array to drop the data into, and assign the
    # axis coordinates, etc.
    if x == 0:
        time_axis = np.linspace(0.0,
            acq_time_ms * 1e-3,
            raw_data.size)
        data = (
            ps.ndshape(
                [raw_data.size, nScans],
                ["t", "nScans"],
            )
            .alloc(dtype=np.complex128)
            .setaxis("t", time_axis)
            .set_units("t", "s")
            .setaxis("nScans", r_[0:nScans])
            .name("signal")
        )
    # }}}
    # drop the data into appropriate index
    data["nScans", x] = raw_data
    sc.stopBoard()
# }}}
data.hdf5_write(
    output_name + ".h5",
    directory=ps.getDATADIR(exp_type="ODNP_NMR_comp/noise_tests"),
) # save data as h5 file

```

S1.11.B. Capturing Receiver Response

The receiver acquired test signal of constant voltage output by the AFG over a set range of frequencies (defined by the user) to obtain the digital filter datasets. Again [S3] interacts with the AFG controlling the USB connection and initialization. Similar to the GDS, an in-house class with methods and attributes was made specifically to interact with the AFG. At each output frequency, the SpinCore acquires a user defined number of scans at a set carrier frequency and spectral width (again defined by the user). Each frequency dataset is saved as a node within an H5 file where the nodename includes the output frequency of the AFG in kHz.

```

from Instruments import AFG
from pyspecdata import r_, ndshape
import time
from numpy import linspace, complex128

```

```

import SpinCore_pp as sc
from datetime import datetime

# {{{ set filename, spectral width and carrier
date = datetime.now().strftime("%y%m%d")
description = "3p9kHz_filter"
SW_kHz = 3.9
output_name = date + "_" + description + ".h5"
carrierFreq_MHz = 14.9
# }}}
# {{{ AFG settings
# Make a list of the desired output frequencies
freq_list = linspace(14.8766e6, 14.9234e6, 300) # Hz
amplitude = 0.01 # desired Vpp
# }}}
# {{{ Spincore settings
adcOffset = 42
tx_phases = r_[0.0, 90.0, 180.0, 270.0]
nScans = 25
nPoints = 1024 * 2
# }}}
with AFG() as a: # context block that automatically
#             handles routines to initiate
#             communication with AFG (arbitrary
#             function generator), perform checks, and
#             to close the (USB serial) connection at
#             the end of the block
a.reset()
for j, frq in enumerate(freq_list):
a[0].output = True # turn on first channel
a.sin(ch=1, V=amplitude, f=frq) # set a sine wave
#                               output with the
#                               desired amplitude
#                               and frequency
time.sleep(2)
for x in range(nScans):
# {{{ configure SpinCore receiver
sc.configureTX(
    adcOffset,
    carrierFreq_MHz,
    tx_phases,
    1.0,
    nPoints,
)
acq_time_ms = sc.configureRX(
    SW_kHz,
    nPoints,
    1,
    1, # assume nEchoes = 1
    1, # assume nPhaseSteps = 1
)
sc.init_ppg()
# }}}
# {{{ ppg to generate the SpinCore Data
sc.load(
    [
        ("marker", "start", 1),
        ("phase_reset", 1),
        ("delay", 0.5e3), # pick short delay (ms)
        ("delay", 10.0),
        ("acquire", acq_time_ms),
        ("delay", 1e4), # short rep_delay_us
        ("jumpto", "start"),
    ]
)
# }}}
sc.stop_ppg()
sc.runBoard()
raw_data = ( # grab data for the single
#             capture as a complex value
sc.getData(
    (2 * nPoints * 1 * 1),
    nPoints,
    1,
    1
)
.astype(float)
.view(complex)
) # assume nEchoes and nPhaseSteps = 1
# {{{ If this is the first scan, then allocate an
# array to drop the data into, and assign the
# axis coordinates, etc.
if x == 0:
time_axis = linspace(0.0,
    acq_time_ms * 1e-3,
    raw_data.size)
data = (
    ndshape(
        [raw_data.size, nScans],
        ["t", "nScans"],
    )
    .alloc(dtype=complex128)
    .setaxis("t", time_axis)
    .set_units("t", "s")
    .setaxis("nScans", r_[0:nScans])
    .name("signal %f kHz" % frq / 1e3)
)
# }}}
# drop the data into appropriate index
data["nScans", x] = raw_data
sc.stopBoard()
data.set_prop(
    "afg_frq", frq / 1e3
) # store the AFG frequency in units of kHz
data.name("afg_%d" % frq) # the nddata name
#                               determines the node name
#                               of the data in the HDF5
#                               file, below
nodename = data.name()
data.hdf5_write(
    output,
    directory="ODNP_NMR_comp/noise_tests",
)

```

S1.11.C. Processing PSDs

The following script calculates the PSD for datasets acquired on the oscilloscope. The final result (unconvolved and convolved) is plotted on a semilog plot. Note it is assumed the acquired data has already been converted to analytic:

```

from numpy import r_
from pyspecdata import (
    figlist_var,
    nddata_hdf5,
    getDATADIR,
)
from pylab import diff, sqrt, ylim, ylabel

width = (
    0.1e6 # width used for Gaussian convolution filter
)
filename = "230914_RX_GDS_4.h5"
nodename = "accumulated_230914"
with figlist_var() as fl:
# load data according to the filename and nodename
s = nddata_hdf5(

```

```

    filename + nodename,
    directory=getDATADIR(
        exp_type="ODNP_NMR_comp/noise_tests"
    ),
)
s.set_units("t", "s")
s = s[
    "ch", 0
] # select the first channel, note multiple
# channels may be acquired
acq_time = diff(s.getaxis("t")[r_[0, -1]])[
    0
] # calculate acquisition time
s.ft("t") #  $\frac{V_p\sqrt{s}}{\sqrt{Hz}}$ 
s /= sqrt(2) # instantaneous  $\frac{V_p\sqrt{s}}{\sqrt{Hz}} \rightarrow \frac{V_{rms}\sqrt{s}}{\sqrt{Hz}}$ 
# {{{ equation 21
s = (
    abs(s) ** 2
) # take mod squared to convert to energy  $\frac{V_{rms}^2}{Hz} \cdot s$ 
s.mean("capture") # average over all captures
s /= acq_time # convert to Power  $\frac{V_{rms}^2}{Hz} = W$ 
s /= 50 # W/Hz
# }}}
s.set_units("t", "Hz")
# Plot unconvolved PSD on a semilog plot
fl.next("", figsize=(6, 4))
fl.plot(
    s["t":(0, 49e6)],
    color="blue",
    label=None,
    alpha=0.1,
    plottype="semilogy",
)
# convolve using the width specified above
# the convolve function of pySpecData automatically
# applies the division by  $\sigma\sqrt{2\pi}$ 
s.convolve("t", width, enforce_causality=False)
# plot the convolved PSD on the semilog plot with the
# unconvolved
fl.plot(
    s["t":(0, 49e6)],
    color="blue",
    label=None,
    alpha=0.3,
    plottype="semilogy",
)
ylim(1e-17, 1.8e-12) # set y limits
ylabel("${S(\nu)} / (W/Hz)")

```

Initially, the raw data acquired on the SpinCore is fed to a pre-processing function. The function performs a Fourier transform of the time domain and the phase cycling dimensions (when applicable) and finally applies the appropriate sinc digital filter (Eq. (22)) before returning the data:

```

import numpy as np
def proc_spincore_generalproc_v1(s, direct="t2",
    include_tau_sub=False):
    """ Preprocessing function that takes the raw data
    and fourier transforms both the time domain into
    the frequency domain and the phase cycling domain
    into the coherence transfer pathway domain. The
    receiver response is also applied prior to
    returning the data.

```

Parameters

=====

s: nddata

Raw dataset that was acquired on the SpinCore.

direct: str

Direct axis of the data.

include_tau_sub: boolean

Option to subtract the echo time in order to center the echo about zero.

Returns

=====

s: nddata

The original data with the receiver response applied returned in the frequency and coherence transfer pathway domain

"""

```

s.run(np.conj) # SC flips data in a weird way,
# this corrects for that
if include_tau_sub: # option to subtract echo time
# to center about zero
    if "tau_us" in s.get_prop("acq_params").keys():
        s[direct] -= (s.get_prop("acq_params")["tau_us"]
            * 1e-6)
s.ft(direct, shift=True)
for j in [k for k in s.dimlabels if k.startswith("ph")]:
    dph = s[j][1] - s[j][0]
    Dph = s[j][-1] + dph - s[j][0]
    if Dph == 1:
        s[j] = (-s[j] + 1) % 1 # when we take the complex
# conjugate, that changes
# the phase cycle, as well,
# so we have to re-label the
# axis coordinates for the
# phase cycle to the negative
# of what they were before.
# We also apply phase wrapping
# to get positive numbers.
    elif Dph == 4: # uses units of quarter cycle
        s[j] = (-s[j] + 4) % 4
    else:
        raise ValueError(
            "the phase cycling dimension "
            + j
            + " appears not to go all the way around"
            + " the circle!"
        )
    s.sort(j)
s.ft([j]) # FT the phase cycling dimensions
# into the coherence transfer
# pathways
# {{{ always put the phase cycling dimensions on the outside
neworder = [j for j in s.dimlabels if j.startswith("ph")]
# }}}
# {{{ reorder the rest based on size
nonphdims = [j for j in s.dimlabels if not
    j.startswith("ph")]
if len(nonphdims) > 1:
    sizeidx = np.argsort([s.shape[j] for j in nonphdims])
    neworder += [nonphdims[j] for j in sizeidx]
# }}}
s.reorder(neworder)
# {{{ apply the receiver response
s.set_prop(
    "dig_filter",
    s.fromaxis(direct).run(
        lambda x: np.sinc(x /
            (s.get_prop("acq_params")["SW_kHz"] *
            1e3))
    ),

```



```

)
s /= s.get_prop("dig_filter") # set the filter
#                               response as a
#                               property so that we
#                               can access at a
#                               later time if
#                               needed
# }}}
s.squeeze()
return s

```

Following the pre-processing, the data is converted to voltage using the acquired calibration factors prior to the calculation of the PSD (Eq. (23)). The final PSD is then plotted (unconvolved and convolved) on a semilog plot using the following script:

```

from numpy import r_
from pyspecdata import figlist_var, find_file
from pyspecProcScripts import lookup_table
from pylab import diff, ylabel, sqrt

width = (
    4e3 # width used for Gaussian convolution filter
)
dg_per_V = 583e6 # calibration coefficient to convert
#               the intrinsic SC units to V. Note this value
#               will change with different SW
filename = "230822_BNC_RX_magon_200kHz.h5"
with figlist_var() as fl:
    # load data and apply preprocessing
    s = find_file(
        filename,
        exp_type="ODNP_NMR_comp/Echoes",
        expno="signal",
        postproc = "spincore_general",
        lookup = lookup_table
    ) # digital filter is applied in preprocessing

```

```

s.rename(
    "nScans", "capture"
) # to be more consistent with the oscilloscope data,
# rename the scans axis
s /= dg_per_V # convert the intrinsic units of the SC
#             into actual Vp
s.set_units("t", "s")
# calculate acquisition time
acq_time = diff(s.getaxis("t")[r_[0, -1]])[0]
s.ft(
    "t", shift=True
) #  $\frac{V_p \sqrt{s}}{\sqrt{Hz}}$ 
s /= sqrt(2) # instantaneous  $\frac{V_p \sqrt{s}}{\sqrt{Hz}} \rightarrow \frac{V_{rms} \sqrt{s}}{\sqrt{Hz}}$ 
# {{{ equation 21
s = (
    abs(s) ** 2
) # take mod squared to convert to energy  $\frac{V_{rms}^2 \cdot s}{Hz}$ 
s.mean("capture") # average over all captures
s /= acq_time # convert to Power  $\frac{V_{rms}^2}{Hz} = W$ 
s /= 50 # W/Hz
# }}}
# plot the unconvolved PSD on a semilog plot
fl.next("", figsize=(6, 4))
fl.plot(
    s, color="blue", alpha=0.1, plottype="semilog"
)
# convolve using the width specified above
# the convolve function of pySpecData automatically
# applies the division by  $\sigma\sqrt{2\pi}$ 
s.convolve("t", width, enforce_causality=False)
# plot the convolved PSD on the semilog plot with the
# unconvolved
fl.plot(
    s, color="blue", alpha=0.5, plottype="semilog"
)
ylabel("${S(\nu)} / (W/Hz)")

```

- [S1] For example, the authors attempted to implement the solution that had been implemented in [S4], by passing the coaxial line through a pass-through BNC grounded to the waveguide, but this actually made the noise worse.
- [S2] J. Mispelter, M. Lupu, and A. Briguët. *NMR Probeheads for Biophysical and Biomedical Experiments: Theoretical Principles and Practical Guidelines (With CD-ROM)*. Imperial College Press and World Scientific Publishing

- co. (2006). ISBN 978-1-86094-637-0 978-1-86094-902-9.
- [S3] J. Franck, A. A. Beaton, and A. Guinness. "Instrument notebook." <https://github.com/jmfrancklab/FLinst> (2017).
- [S4] J. M. Franck, A. Pavlova, J. A. Scott, and S. Han. "Quantitative Cw Overhauser Effect Dynamic Nuclear Polarization for the Analysis of Local Water Dynamics." *Progress in Nuclear Magnetic Resonance Spectroscopy*, 74:33–56 (2013). doi:10.1016/j.pnmrs.2013.06.001.